

Vertical Convergence of Turbulent and Double-Diffusive Heat Flux Drives Warming and Erosion of Antarctic Winter Water in Summer

I. S. GIDDY^{a,b,c}, I. FER^{d,e}, S. SWART^{a,b} AND S.-A. NICHOLSON^c

^a Department of Marine Sciences, University of Gothenburg, Gothenburg, Sweden

^b Department of Oceanography, University of Cape Town, Cape Town, South Africa

^c Southern Ocean Carbon-Climate Observatory, CSIR, Cape Town, South Africa

^d Geophysical Institute, University of Bergen, Bergen, Norway

^e Bjerknes Center for Climate Research, Bergen, Norway

(Manuscript received 21 December 2022, in final form 6 May 2023, accepted 8 May 2023)

ABSTRACT: The seasonal warming of Antarctic Winter Water (WW) is a key process that occurs along the path of deep water transformation to intermediate waters. These intermediate waters then enter the upper branch of the circumpolar overturning circulation. Despite its importance, the driving mechanisms that mediate the warming of Antarctic WW remain unknown, and their quantitative evaluation is lacking. Using 38 days of glider measurements of microstructure shear, we characterize the rate of turbulent dissipation and its drivers over a summer season in the northern Weddell Sea. Observed dissipation rates in the surface layer are mainly forced by winds and explained by the stress scaling ($r^2 = 0.84$). However, mixing to the base of the mixed layer during strong wind events is suppressed by vertical stratification from sea ice melt. Between the WW layer and the warm and saline circumpolar deep water, a subsurface layer of enhanced dissipation is maintained by double-diffusive convection (DDC). We develop a WW layer temperature budget and show that a warming trend (0.2°C over 28 days) is driven by a convergence of heat flux through mechanically driven mixing at the base of the mixed layer and DDC at the base of the WW layer. Notably, excluding the contribution from DDC results in an underestimation of WW warming by 23%, highlighting the importance of adequately representing DDC in ocean models. These results further suggest that an increase in storm intensity and frequency during summer could increase the rate of warming of WW with implications for rates of upper-ocean water mass transformation.


SIGNIFICANCE STATEMENT: Around Antarctica, the summer warming of the subsurface cold Antarctic Winter Water feeds the upper layer of the overturning circulation. This study aims to quantify the mechanisms that mediate the warming of Antarctic Winter Water. Our results reveal that the observed warming of this layer can be explained by both surface wind-driven mixing processes as well as double-diffusive convection occurring beneath the Winter Water layer. Understanding the role of these mechanisms is important for understanding the regions upper-ocean heat distribution, the rates of water mass transformation and how they might respond to changes in sea ice, stratification, and the overlying large-scale winds.

KEYWORDS: Southern Ocean; Diapycnal mixing; Turbulence; Heat budgets/fluxes; Small-scale processes

1. Introduction

A unique characteristic of polar ocean regions is the formation of Winter Water (WW) through intense heat loss to the atmosphere and sea ice freezing. In summer, the seasonally present subsurface WW acts as a barrier between the atmosphere and deep water sources of heat and carbon, thereby modulating the direct exchange of heat and carbon between the atmosphere and ocean interior. South of the Antarctic Polar Front (APF), cold subsurface Antarctic WW (with a nominal depth range of ~50–400 m; Toole 1981) forms an inversion separating the warm surface water from the warm, CO₂-rich upper Circumpolar Deep Water (UCDW, with

nominal depth range of ~150–1500 m; Foster and Carmack 1976). Here UCDW upwells toward the surface, where it is transformed by air–sea ice buoyancy fluxes, thereafter subsiding as part of the upper branch of the meridional overturning circulation (Abernathey et al. 2016; Pellichero et al. 2018). The along-isopycnal link between the deep ocean and the surface in this region means that changes in the physical drivers of upper-ocean properties, and therefore the rate of water mass transformation, can have global implications. The rate of water mass transformation in the upper ocean has been linked to the transport and melt of sea ice (Abernathey et al. 2016), which increases the buoyancy of surface waters before they enter the upper branch of the overturning circulation. Below the mixed layer, the exchange of water properties between the mixed layer and UCDW, across the Antarctic WW layer plays an important part in the transformation of UCDW to Antarctic Intermediate Water (AAIW) during summer (Evans et al. 2018). Thus, understanding the processes that form and modify WW is of global climatic relevance.

 Denotes content that is immediately available upon publication as open access.

Corresponding author: I. S. Giddy, isabelle.giddy@gu.se

DOI: 10.1175/JPO-D-22-0259.1

© 2023 American Meteorological Society. This published article is licensed under the terms of a Creative Commons Attribution 4.0 International (CC BY 4.0) License



WW is formed during cold winter months under destabilizing buoyancy forcing through cooling and sea ice growth. During these months, the surface mixed layer cools and deepens, entraining underlying deep waters (UCDW; Foster and Carmack 1976; Hoppema 2004) and resulting in vertical fluxes of heat and salt (Gordon and Huber 1984; Martinson 1990; Evans et al. 2018). If the mixed layer cools sufficiently for sea ice formation, subsequent brine rejection during sea ice growth will increase the density of the mixed layer and entrain more heat from below, which will in turn warm the mixed layer further. This balance limits the volume of sea ice that can form, maintaining a relatively thin layer (~ 0.5 m) of sea ice across the subpolar Southern Ocean (Gordon and Huber 1990; Shaw and Stanton 2014). The interplay between surface cooling and sea ice formation with the resultant upward heat fluxes also limits the depth of surface mixing, confining the mixed layer to the upper 200 m (Gordon and Huber 1990; Pellichero et al. 2017; Wilson et al. 2019). Further, there is regional heterogeneity in the coupling between winter ice growth and the entrainment of heat into the mixed layer. Regions with stronger stratification (e.g., the Ross Sea), require far greater sea ice formation (i.e., brine rejection) before sufficient heat is entrained to erode the pycnocline. In contrast, in the Weddell Sea, which has characteristically weak stratification and a sharp thermocline, the pycnocline is easily eroded by a relatively small amount of sea ice growth (0.5–1.5 m), favoring a high rate of wintertime heat ventilation with a strong negative feedback to ice growth, as observed by Shaw and Stanton (2014).

During winter, the warmer and saltier UCDW mixes into the surface mixed layer, which causes it to cool down. This cooler water then becomes WW during summer and is saltier and colder than the overlying freshwater. In summer, the WW is capped beneath the surface layer and begins to warm up. As it warms, it also freshens and becomes less dense, eventually transforming into AAIW. During austral summer, WW is identified as a local subsurface temperature minimum that is capped between the warm, fresh surface waters and the underlying warm and salty UCDW (Toole 1981; Gordon and Huber 1990; Evans et al. 2018; Sabu et al. 2020). The depth of the temperature minimum ranges from ~ 300 m near the Polar Front to shallower depths (~ 50 m) with proximity to the Antarctic continent, where sea ice melt additionally stratifies the upper ocean (Toole 1981). Evans et al. (2018) show that the seasonal transitions of WW formation and progression, and its role in UCDW transformation, is driven both by air–ice–sea buoyancy fluxes at the surface and mixing at the subsurface. They attribute the wintertime transformation of dense water into lighter upper-ocean mixed layer water to the action of cabbeling (in which two water parcels mix to form a denser water parcel) at the subsurface between salty, cold mixed layer waters and the warm and salty UCDW. The summertime transformation is attributed to heat exchange with the atmosphere and sea ice melt. While Evans et al. (2018) addressed the processes driving the transformation of UCDW to AAIW at basin scales, the surface and subsurface mixing processes were not explicitly observed. Ultimately, water properties are irreversibly mixed at the scale of dissipation. Here, we use direct observations of dissipation to attribute the drivers of and quantify the rate of surface and subsurface

mixing processes that control the transformation of WW to AAIW during austral summer.

The main sources of turbulence production in the surface ocean are convection, winds, and waves. In the summer, the surface buoyancy fluxes are typically stabilizing (positive into the ocean) through surface warming and sea ice melt (Pellichero et al. 2017; Giddy et al. 2021). Thus, the remaining sources of turbulence production at the surface are primarily from winds and waves (Belcher et al. 2012). Wind- and wave-driven shear production is prevalent in the Southern Ocean in all seasons (Belcher et al. 2012). Mixing due to wind-driven shear production in the surface mixed layer is important in driving fluxes of carbon between UCDW and the mixed layer (e.g., Song et al. 2019; Nicholson et al. 2022). Processes that drive enhanced wind-driven shear above the cold WW may result in substantial heat exchange, increasing the rate of warming and erosion of the WW. Indeed, WW properties in the Southern Ocean vary zonally over summer in both temperature and thickness (Fig. 1; Sabu et al. 2020), responding to changes in wind forcing (Anilkumar et al. 2006) and large-scale atmospheric variability [e.g., Southern Annular Mode (SAM)]. Stronger winds and a positive SAM promote enhanced warming of WW, likely through shear-driven mixing in the mixed layer (Sabu et al. 2020).

The possible subsurface mixing processes are shear instabilities from background shear and breaking internal waves. Additionally, in polar oceans, the vertical thermohaline structure preconditions the ocean to double-diffusive convection (DDC; van der Boog et al. 2021). DDC was shown to be present at the base of the WW where warm, salty water underlies cooler, fresher water (Shaw and Stanton 2014; Bebieva and Speer 2019). However, its contribution to the warming of the WW layer is not known in summer. DDC can occur when gravitationally stable colder, and fresher water, overlies warmer, saltier water. At a molecular level, heat diffuses approximately 100 times faster than salt in seawater. Thus, if a parcel of fluid is displaced downward, it will quickly absorb heat by diffusion from its surroundings and “overshoot” when rising back through the medium. This leads to an oscillation of growing amplitude and convecting cells, ultimately forming well-mixed layers separated by thin interfaces with temperature and salinity steps. The vertical structure is visible as characteristic layering or staircases in the temperature and salinity profiles when background turbulent mixing is sufficiently weak to allow the formation of the layer (Bebieva and Timmermans 2016; Shaw and Stanton 2014; Shibley et al. 2017). The resultant convection can lead to elevated rates of dissipation. Notably, the convecting cells can effectively exchange heat and salt across the interface because all potential energy (PE) is used to produce turbulent kinetic energy (TKE; St. Laurent and Schmitt 1999; Inoue et al. 2007). This differs from shear-driven turbulence production wherein a proportion of TKE (~ 0.2 ; Osborn 1980) is expended in raising the PE of the water parcel and driving a buoyancy flux under stable stratification. An outstanding question pertains to the role of DDC in ice free summertime conditions and its contribution to the observed thinning and warming of WW.

The aforementioned mixing processes may drive modifications to WW through the summer via turbulence production in the surface and subsurface. The primary goal of this study is to

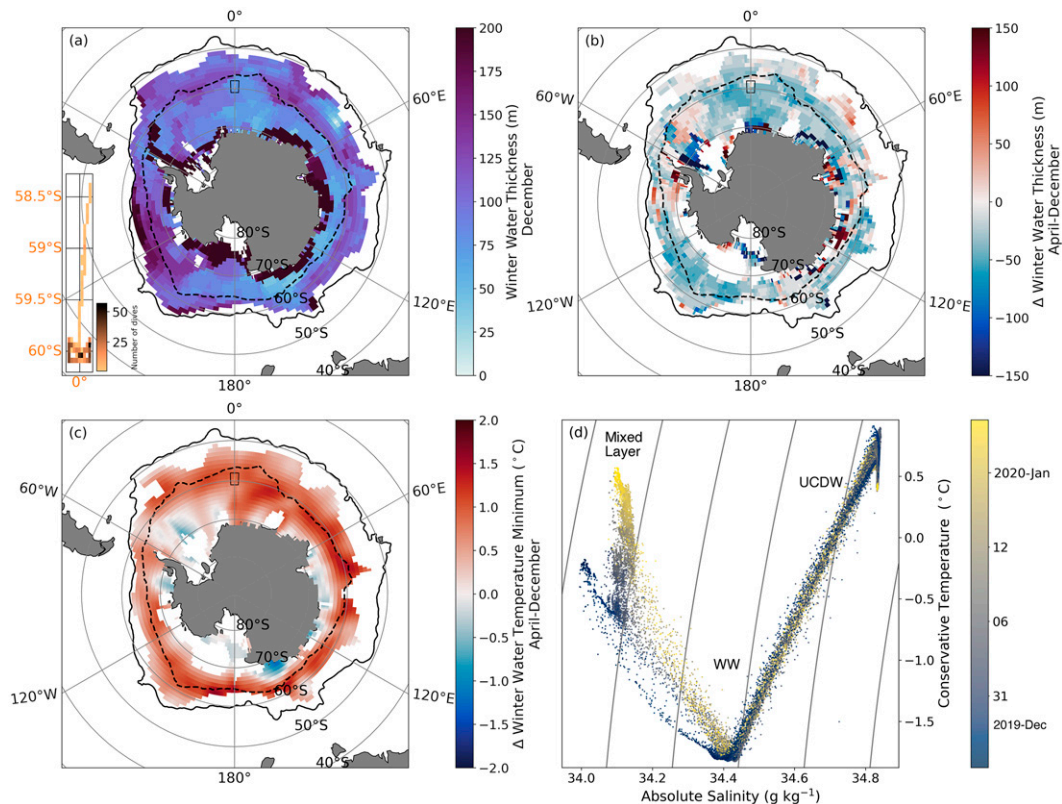


FIG. 1. (a) Distribution of Antarctic Winter Water (subsurface temperature minimum layer; WW) and the location of the glider (black-outlined box at 60°S, 0°) deployed from December 2019 to February 2020. The inset shows the glider “bow-tie” sampling pattern colored by dive density. The shading depicts December climatological WW thickness derived from EN4 (2010–20; Good et al. 2013). (b) The seasonal progression of the thickness of WW (i.e., the difference between April and December climatologies). (c) The seasonal progression of the WW minimum temperature between December and April climatologies. WW that is completely eroded by April is not shown in (b) and (c). The mean (1993–2012) location of the Antarctic Polar Front (solid black line; Park and Durand 2019) and the median (1981–2010) September sea ice extent (black dashed line; National Snow and Ice Data Center) are overlaid. (d) Glider-observed temperature and salinity plot colored by time, highlighting the summer seasonal progression of thermohaline properties of the mixed layer, WW, and Upper Circumpolar Deep Water (UCDW).

investigate the role of turbulent mixing in the transformation of WW during summer using 38 days of direct observations of turbulent dissipation in the Weddell Sea. We 1) present a detailed characterization of turbulent dissipation, 2) confirm the likely sources of turbulence, 3) quantify mean vertical heat fluxes, and 4) determine the contribution of diapycnal heat fluxes to the seasonal warming of the WW and therefore the processes that may increase or reduce the rate of transformation of WW.

2. Data and methods

a. Slocum glider

A 1000-m-rated Teledyne Webb Research Slocum G2 electric ocean glider was deployed from the research vessel SA *Agulhas II* at 58°S, 0° on 17 December 2019. The glider then transited directly south for 10 days covering a distance of ~224 km, until it reached 60°S on 25 December 2019. Thereafter, the glider completed a bow-tie pattern of shorter transits (~20–60 km) until it was retrieved on 18 February 2020

(see inset on Fig. 1a). The glider dived to 1000 m, collecting measurements during its dives and climbs at a typical vertical resolution of 0.5 m. The typical separation between start of subsequent dives was between 3.5 and 5 km, and the average dive and climb angle was 25°.

The glider was fitted with a Sea-Bird Slocum Glider Payload conductivity–temperature–depth sensor (GPCTD). On 24 January 2020 the CT pump failed because of a blockage, rendering the salinity data thereafter unusable until it unblocked on 10 February 2020. For the purposes of this study, we elected to truncate the data at this point, and only included data until 24 January 2020, resulting in 38 days of continuous 1-s-resolution temperature, salinity, and pressure observations. The glider data were processed using the software developed by G. Krahnmann (GEOMAR; Krahnmann 2023). This includes correction for thermal inertia of the conductivity cell and a hydrodynamic model from which the angle of attack and flow rate past the sensor are computed. Temperature and salinity measurements were compared with in situ CTD casts during deployment and retrieval of the glider. No

correction was applied to temperature, but salinity was corrected for an initial offset of $+0.0125 \text{ g kg}^{-1}$ and a linear drift of $-3.8 \times 10^{-4} \text{ g kg}^{-1} \text{ day}^{-1}$ over the full deployment.

b. Microstructure

Ocean microstructure data were collected using a neutrally buoyant, low-power, self-contained turbulence instrument package MicroRider-1000LP (MR), manufactured by Rockland Scientific International. The MR was attached to the top of the glider with turbulence sensors protruding at the front, and was equipped with two airfoil velocity shear probes (SPM-38) oriented orthogonal to each other such that shear probe 1 (shear probe 2) was sensitive to perturbations in the vertical (horizontal) direction relative to the direction of travel of the glider ($\partial w/\partial x$ and $\partial v/\partial x$, respectively), a pressure transducer, a two-axis vibration sensor (a pair of piezo-accelerometers), and a high-accuracy dual-axis inclinometer (ADIS 16209, pitch and roll angles accurate to 0.18°). Shear microstructure measurements were made to 500 m on both climbs and dives throughout the deployment. The sampling frequency is 512 Hz on all turbulence channels (vibration and shear) and 64 Hz for the other channels (pitch, roll, and pressure).

The viscous dissipation rate of TKE per unit mass (dissipation hereinafter) is derived from the shear microstructure following Fer et al. (2014) and the recommendations of the SCOR Working Group on analyzing ocean turbulence observations to quantify mixing (ATOMIX; <http://wiki.uib.no/atomix>). The record from each shear probe is segmented into half-overlapping 30 s long portions for spectral analysis. A fast Fourier transform (FFT) length corresponding to 5 s is chosen, and each 5-s segment is detrended and Hanning windowed before calculating the spectra. The average speed through the water, or equivalently, the flow past the MR sensor U_p , was 0.37 m s^{-1} during the deployment. We use this value, together with the size of the glider ($\sim 2 \text{ m}$) to determine the time interval over which to calculate the rate of dissipation, noting that the FFT length should not be greater than the length of the platform. For statistical reliability the ratio of dissipation length to FFT length should never be less than 2. We elected to use the 30-s interval, with a 5-s FFT length and 50% overlap (15 s), which gives 5 degrees of freedom. This selection is equivalent to 1.8 m along the path-length and resolves the low-wavenumber part of the spectrum that is crucial for the roll off for low dissipation rates. The shear probe signal coherent with the accelerometer data (from the two-axis vibration sensor) is removed using the method outlined in Goodman et al. (2006). The frequency spectra are converted into along-path wavenumber k spectra using Taylor's frozen field turbulence hypothesis and U_p . The dissipation rate for each segment is then calculated, assuming isotropic turbulence, by integrating the wavenumber spectrum as

$$\varepsilon_j = \frac{15}{2} \nu \overline{\left(\frac{\partial u_j}{\partial x}\right)^2} \approx \frac{15}{2} \nu \int_{k_i}^{k_u} \Psi(k) dk, \quad (1)$$

where $\partial u_j/\partial x$ is the turbulent scale shear component measured along the glider's along-path coordinate x , j identifies the shear

probe number oriented orthogonal to measure the transverse and vertical components of the along-path shear, ν is the kinematic viscosity of seawater, which is a function of the local water temperature, and the overbar denotes averaging. The shear wavenumber spectrum Ψ is integrated between k_l , set by the window length, and k_u , the minimum in a curve fit to the shear spectrum, which is unaffected by noise. The empirical model for the turbulence spectrum, determined by Nasmyth (1970), is used to correct for unresolved variance below and above the integration limits.

Following the initial estimation of dissipation a number of quality control steps were applied, detailed in appendix A. The final dissipation estimation is the average of independent estimates computed from each shear probe. After quality control, 49% of the ε estimates from shear probe 1 and 83% from shear probe 2 were retained. The average resulted in 88% of possible segments being retained. The noise floor for ε is determined to be lower than $10^{-11} \text{ W kg}^{-1}$.

c. Ancillary data

Additional data products are used together with the glider data to estimate and characterize the surface forcing and ocean dynamics for the region. Collocated zonal and meridional wind stress as well as sensible, latent, shortwave, and longwave heat fluxes together with evaporation and precipitation, were retrieved from the fifth major global reanalysis produced by ECMWF (ERA5) at hourly intervals, with a $0.25^\circ \times 0.25^\circ$ resolution (Hersbach et al. 2018). EN4 (version 4.2.2, objective analyses; Good et al. 2013) climatology (2010–20), with bias corrections (Cheng et al. 2014; Gouretski and Cheng 2020) is used to produce the WW maps in Fig. 1.

d. Surface buoyancy and momentum fluxes

Net surface buoyancy flux into the ocean is defined as

$$B_o = -g \left[\frac{\alpha Q_{\text{net}}}{\rho c_p} + \beta S(E - P) \right], \quad (2)$$

where $g = 9.8 \text{ m s}^{-2}$ is gravitational acceleration, α is the thermal expansion coefficient computed from Absolute Salinity and Conservative Temperature using the Gibbs SeaWater TEOS-10 Toolbox (McDougall and Barker 2011), Q_{net} is the net heat flux into the ocean (shortwave + longwave + latent + sensible), c_p is the heat capacity of water = $4000 \text{ J K}^{-1} \text{ kg}^{-1}$, $\rho_0 = 1027 \text{ kg m}^{-3}$ is a reference density, β is the saline contraction coefficient, E is evaporation, P is precipitation, and S is surface salinity measured by the glider.

e. Water mass and layer definitions

The water mass layers are defined as follows. The mixing layer depth is derived from estimates of turbulent dissipation following Brainerd and Gregg (1995), where active mixing occurs above a threshold of $\varepsilon = 10^{-8} \text{ W kg}^{-1}$. The mixed layer depth is defined based on a change in density of 0.03 kg m^{-3} from a reference depth of 10 m (de Boyer Montégut et al. 2004). WW in the austral summer is defined as a subsurface temperature minimum. The base of the WW is identified as the local maximum of the temperature gradient below the WW temperature minimum. The thickness of the WW layer is defined as the difference

between the base of the mixed layer and the maximum temperature gradient below the WW temperature minimum (similar to the peak stratification). A transition layer (TL) between WW and UCDW is defined as the region of high stratification below the WW, with the boundary identified as the base of the WW (as in [Dohan and Davis 2011](#)). Beneath the TL lies the UCDW.

f. Derivation of turbulence parameters

The turbulent buoyancy or heat flux can be expressed as a downgradient mixing of background density or temperature gradients at a rate given by a diapycnal eddy diffusivity K . Diapycnal diffusivity is estimated from measurements of turbulent viscous dissipation following the [Osborn \(1980\)](#) model for mixing in a stratified ocean,

$$K = \Gamma \frac{\varepsilon}{N^2}, \quad (3)$$

where Γ is the mixing coefficient related to mixing efficiency ([Gregg et al. 2018](#)), ε is viscous dissipation, and N is the Brunt–Väisälä frequency, calculated using the Gibbs Seawater TEOS-10 Toolbox ([McDougall and Barker 2011](#)).

The mixing coefficient Γ indicates the conversion efficiency of TKE into PE and is assumed, at its upper limit, to be a constant, 0.2. However, the mixing efficiency varies depending on the intensity of mixing. Turbulence intensity is measured using the Reynolds buoyancy number Re , which quantifies the energetic capacity of the stratified flow to develop vertical overturns that lead to diapycnal mixing:

$$Re = \frac{\varepsilon}{\nu N^2}, \quad (4)$$

where $\nu = 1.8 \times 10^{-6} \text{ m}^2 \text{ s}^{-1}$ is the kinematic viscosity.

At high or low mixing intensities the mixing coefficient decreases ([Gregg et al. 2018](#)). [Bouffard and Boegman \(2013\)](#) categorize four mixing regimes as a function of the Reynolds buoyancy number to estimate diapycnal diffusivity depending on the turbulence intensity: molecular, buoyancy-controlled, transitional, and energetic, the thresholds of which are determined from observations. In the molecular regime diffusivity is set to molecular diffusivity. The buoyancy-controlled regime accounts for turbulent diffusivity at low Reynolds numbers where molecular diffusivity is still important and mixing is less efficient for salinity than for temperature. The transitional regime refers to the traditional [Osborn \(1980\)](#) model where $\Gamma = 0.2$, and the energetic regime accounts for a decrease in mixing efficiency at high Reynolds numbers due to weak density gradients. These regimes, within the context of the observations, are marked in [Fig. 3](#) and are used to select the appropriate mixing coefficient for each estimate of eddy diffusivity.

The above holds for conditions where shear is the source of turbulent production, however because DDC is driven by the release of PE, the production term of the TKE budget is dominated by the destabilizing buoyancy flux such that the mixing coefficient can be assumed to be close to 1 ([St. Laurent and Schmitt 1999](#)). Later, we discuss the implications to heat fluxes if mixing in the TL can be assumed to be driven by DDC and a mixing coefficient of 1 is applied to [Eq. \(3\)](#).

Further, by assuming the eddy diffusivity of density is equivalent to the eddy diffusivity of temperature, the vertical flux of heat (positive upward) can be defined as

$$F_H = -\rho_0 c_p K \frac{\partial T}{\partial z}, \quad (5)$$

where K is the diapycnal eddy diffusivity and $\partial T/\partial z$ is the vertical gradient in temperature with depth. We use the gradient in temperature and density computed over 3 m.

g. Double-diffusive convection

Double-diffusive convection is an efficient mechanism for heat and salt transport in the ocean. The potential for DDC to occur is assessed using the density ratio R_ρ , defined here as

$$R_\rho = \frac{\alpha \Delta T}{\beta \Delta S}, \quad (6)$$

in which $\Delta T/\Delta S$ is the ratio of the bulk vertical gradients of temperature and salinity, estimated as the difference in temperature and salinity between the adjacent layers.

The density ratio can be mapped onto polar coordinates to give the Turner angle ([Turner 1973](#)):

$$Tu = \tan^{-1} \left(\alpha \frac{\partial T}{\partial z} - \beta \frac{\partial S}{\partial z}, \alpha \frac{\partial T}{\partial z} + \beta \frac{\partial S}{\partial z} \right). \quad (7)$$

When Tu is less than $-\pi/4$ and greater than $-\pi/2$, the water column is susceptible to DDC, with values closer to $-\pi/4$ experiencing stronger DDC.

The potential for DDC is additionally estimated following [Middleton et al. \(2021\)](#). The central hypothesis of this method is that the compensated thermohaline variance (spice) is transferred downscale by along-isopycnal stirring until it reaches a scale where the upgradient buoyancy flux drives double-diffusive motions. The local along-isopycnal spice variance from a temperature–salinity (T – S) section is extrapolated to the scale of 3D turbulence based on the Ozmidov length scale and using a model spectrum with a slope of k^{-1} [see [Eq. \(B1\)](#)]. We apply the method to each glider north–south transect individually. An example transect is given in [appendix B](#).

3. Results

a. Observations of summertime warming and erosion of Antarctic Winter Water

During austral summer, the subpolar Southern Ocean (south of the APF) is characterized by the widespread presence of subsurface WW ([Figs. 1a–c](#)). The thickness of the WW in December (111 ± 60 m), which is ultimately an indication of the extent of the barrier between the surface mixed layer and the deeper interior heat and carbon reservoirs, is spatially heterogeneous. In December, the thickest WW layers are located close to the ice shelf (~ 200 m; [Fig. 1a](#)). The rate of erosion or thinning and warming of the WW layer over the summer season is also widespread but heterogeneous ([Figs. 1b,c](#)).

In situ glider observations, which are carried out in a region where on average WW thickness erodes in summer (by ~ 50 m;

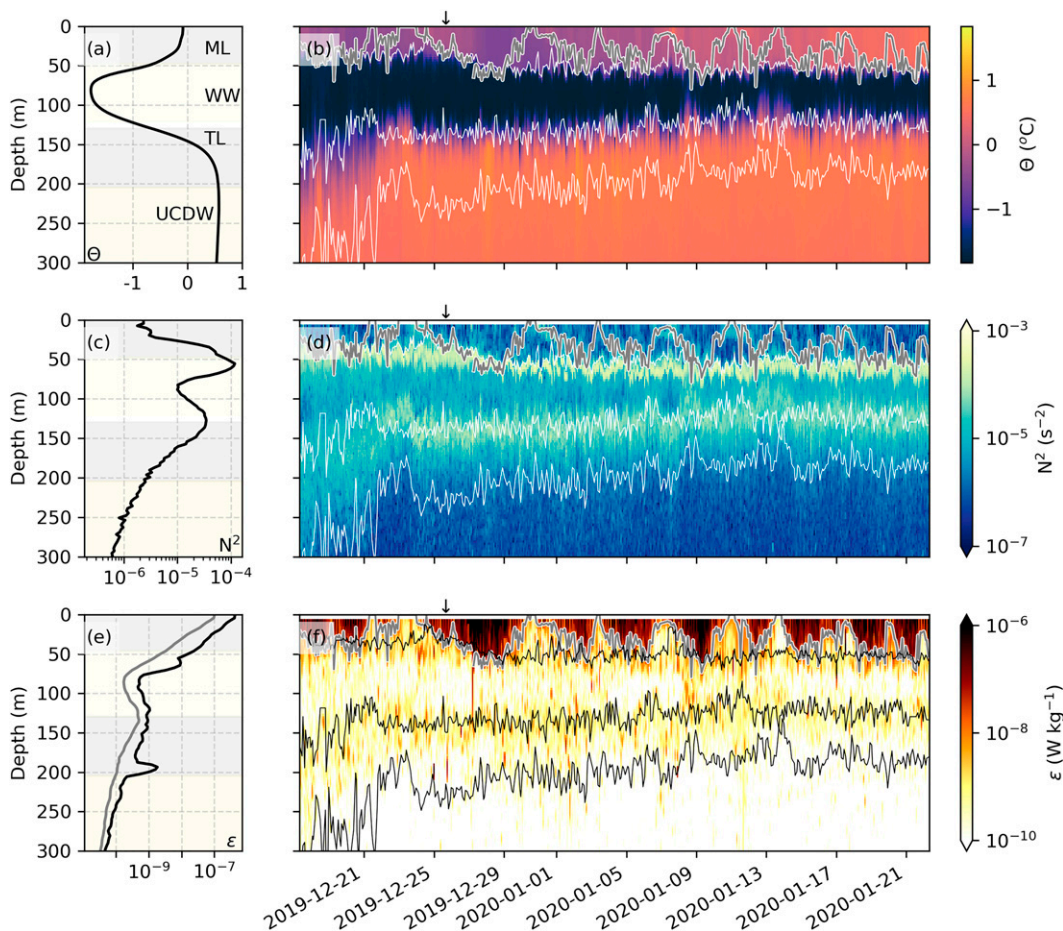


FIG. 2. (a),(c),(e) Mean and (b),(d),(f) temporal evolution of (top) Conservative Temperature Θ , (middle) stratification N^2 , and (bottom) turbulent dissipation ε . The gray line in (e) is the geometric mean. From the surface to depth, the extent of the mixing layer, the mixed layer (ML), the WW, and the transition layer (TL) are contoured in (b), (d), and (f). The gray and yellow shading in (a), (c), and (e) indicates the time-averaged vertical extents of the ML, the WW, the TL, and the UCDW. The black arrow in (b), (d), and (f) indicates when the bow-tie sampling pattern begins.

Fig. 1b), provide a high-resolution perspective of the seasonal evolution of the vertical structure of the upper ocean in this region. The water column at the glider location in the northeast Weddell Sea is composed of three distinct water masses identified in temperature and salinity space (Fig. 1d): the surface mixed layer (ML), the WW characterized by the temperature minimum and the deep warm and saline UCDW. The surface waters and WW showed an increase in temperature during austral summer, over the course of the glider deployment (Fig. 1d).

The subsurface temperature minimum that identifies the WW is again evident in the time-averaged vertical profile of temperature (Fig. 2a). Recent sea ice melt caps the cold, salty surface water that formed during winter with a shallow, fresh layer that rapidly warms under positive heat fluxes from the atmosphere (see Fig. 4a, introduced later). The combination of these stabilizing buoyancy fluxes results in a strongly stratified mixed layer (Figs. 2b–d). Strong, but intermittent mixing in the surface mixed layer is evident from the high values of dissipation [$O(10^{-6}) \text{ W kg}^{-1}$].

b. Rates of turbulent dissipation

The distribution of turbulent dissipation rates is skewed to the right (Fig. 3a), spanning several orders of magnitude from 10^{-12} to $10^{-6} \text{ W kg}^{-1}$, with 63% of the observations measured in quiescent conditions ($\varepsilon < 10^{-10} \text{ W kg}^{-1}$) and only 3% greater than $10^{-7} \text{ W kg}^{-1}$. Rates of dissipation also vary with depth (Figs. 2b and 3a, Table 1). The highest rates ($1.9 \times 10^{-8} \text{ W kg}^{-1}$; geometric mean) of dissipation occur at the surface, where the ocean is in direct contact with the atmosphere and subject to mechanical forcing by winds and waves. There is a secondary region of enhanced dissipation rates at the base of the subsurface WW and within the transition layer (geometric means for the WW layer and transition layer are 3.7×10^{-10} and $2.0 \times 10^{-10} \text{ W kg}^{-1}$, respectively). Below the transition layer the geometric mean dissipation rate is $3.0 \times 10^{-11} \text{ W kg}^{-1}$.

The buoyancy Reynolds number (Fig. 3b) quantifies the energetic capacity of the stratified flow to develop vertical overturns that lead to diapycnal mixing. It is defined as the ratio of turbulent kinetic energy given by dissipation, which would lead to

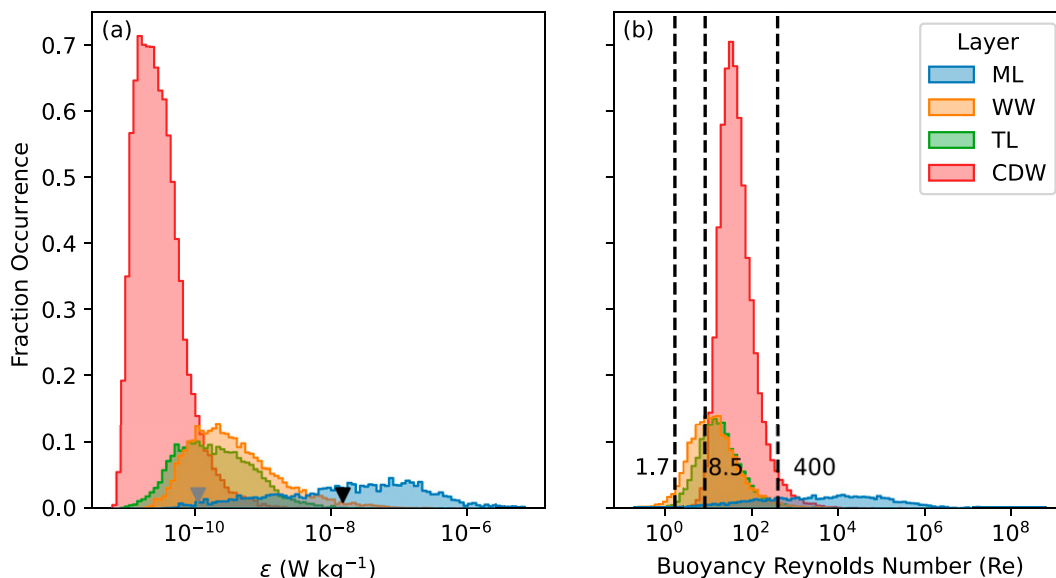


FIG. 3. (a) Layered histogram of turbulent dissipation separated into upper-ocean layers: mixed layer, Antarctic Winter Water, transition layer, and Upper Circumpolar Deep Water. Inverted triangles identify the geometric mean (gray) and arithmetic mean (black) of the complete dataset. (b) Distribution of the buoyancy Reynolds number Re , also separated by layers. Vertical lines identify the thresholds for mixing regimes that are used to derive diapycnal diffusivity K (Bouffard and Boegman 2013).

vertical overturns, to the potential energy stored in stratification, which tends to inhibit overturns. Typically, a critical value of $Re \sim 10$ is assumed, below which diapycnal turbulent mixing is unlikely (Shih et al. 2005; Bouffard and Boegman 2013). While a large number of measurements recorded low values of dissipation, 83% of the measurements occurred under conditions where $Re \geq 10$, suggesting that in most cases, stratification was not sufficiently strong to inhibit even weak vertical overturns. This shows that vertical fluxes of properties such as heat and carbon are largely set by turbulent mixing rather than molecular diffusion. This is different than the more quiescent Arctic

marginal ice zone (Fer et al. 2010; Scheifele et al. 2021), which is also impacted by positive buoyancy during ice melt but does not experience the strong wind forcing that is characteristic of the Southern Ocean (Young and Ribal 2019).

c. Mixing processes

Here we present evidence for the primary drivers of summertime turbulent dissipation in the upper subpolar Southern Ocean. The motivation for this is twofold. First, different turbulent regimes (e.g., shear production versus DDC) are associated with different mixing efficiencies, which will impact vertical

TABLE 1. Statistics of 3-m vertically averaged turbulent parameters. Here, AM indicates arithmetic mean and GM is geometric mean.

		ε (W kg^{-1})	Re	K ($\text{m}^2 \text{s}^{-1}$)	Count
All	AM	1.5×10^{-8}	6243	1×10^{-4}	80 355
	GM	1.1×10^{-10}	—	9.4×10^{-6}	
	Median	5.4×10^{-11}	32	9.5×10^{-6}	
Mixed layer	AM	1.5×10^{-7}	72 107	—	7734
	GM	1.9×10^{-8}	—	—	
	Median	2.5×10^{-8}	1218	—	
Winter Water	AM	2.8×10^{-9}	57	1.3×10^{-5}	12 843
	GM	3.7×10^{-10}	—	3.5×10^{-6}	
	Median	2.8×10^{-10}	13	4×10^{-6}	
Transition layer	AM	7.3×10^{-10}	202	1.5×10^{-5}	11 549
	GM	2.0×10^{-10}	—	5.1×10^{-6}	
	Median	1.8×10^{-10}	17	5×10^{-6}	
Upper Circumpolar Deep Water	AM	6.0×10^{-11}	107	2.4×10^{-5}	47 229
	GM	3.0×10^{-11}	—	1.1×10^{-5}	
	Median	2.7×10^{-11}	39	1.2×10^{-5}	

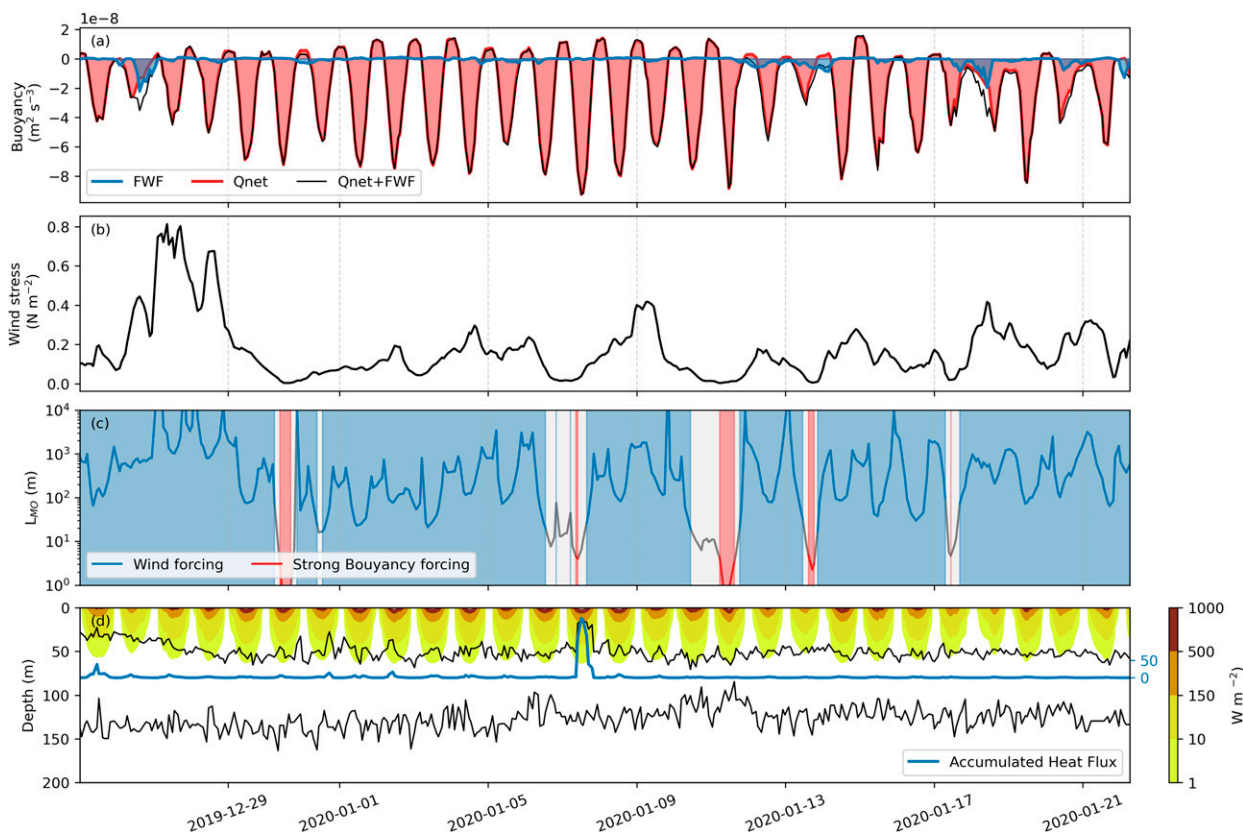


FIG. 4. Time series (25 Dec 2019–22 Jan 2020) of surface fluxes at 60°S, 0°: (a) Net surface buoyancy flux (black, positive upward), decomposed into freshwater (blue) and heat (red) components. (b) Wind stress. (c) Monin–Obukhov length scale L_{MO} , plotted on a log scale. Color shading identifies wind-driven (blue; $z/L_{MO} < 0.3$), strong buoyancy-driven (red; $z/L_{MO} > 1$) and mixed wind and buoyancy (gray; $0.3 > z/L_{MO} > 1$) regimes at $z = 5$. (d) Decay with depth of incoming shortwave radiation. The vertical sum of shortwave radiation into the WW layer is overlaid in blue. Black contours show the mixed layer and the base of the WW layer.

heat fluxes. Second, an understanding of the drivers of turbulent mixing is essential for the interpretation of the variability in the mixing itself.

Surface buoyancy forcing is largely stabilizing (negative out of the ocean), except during nighttime (Fig. 4a), such that wind becomes a major source of turbulence in the surface ocean. The Monin–Obukhov length scale is used to determine the relative importance of wind forcing to buoyancy forcing and defined as

$$L_{MO} = \frac{-u_*^3}{\kappa B_o}, \quad (8)$$

where u_* is the friction velocity defined as $\sqrt{\tau/\rho_o}$, τ is wind stress, κ is the von Kármán constant, and B_o is the surface buoyancy flux. The L_{MO} has a large dynamic range (>1000 m under strong winds and <1 m under weak winds and stabilizing buoyancy forcing with negative B_o) (Figs. 4b,c).

1) MECHANICALLY DRIVEN MIXING

The possible sources of shear in the surface layer and immediately below the mixed layer are shear resulting from

geostrophic current, and winds and inertial oscillations. Deeper below the base of the mixed layer, possible sources are geostrophic currents and internal waves.

We assess the potential importance of geostrophic shear in producing turbulence by estimating the thermal wind shear, $\partial u_g/\partial z = g(\partial\rho/\partial y)/f$, from temperature and salinity measured by the glider. We assume that the glider is mostly measuring the meridional density gradient (see glider sampling pattern in Fig. 1a). While some shear due to geostrophic currents was present, shear was low relative to local stratification and therefore geostrophic shear production of turbulence between the layer interfaces was likely negligible [$(\partial u_g/\partial z)^2 \sim O(10^{-7} \text{ s}^{-2})$; $N^2 \sim O(10^{-5} \text{ s}^{-2})$]. This is unsurprising given that the region is relatively quiescent in terms of larger-scale currents (du Plessis et al. 2022, their Fig. 1a).

We estimate dissipation attributed to internal waves in the ocean interior using the strain-based finescale parameterization for dissipation (Polzin et al. 1995; Whalen et al. 2015), over 64 m half-overlapping vertical bins. The time-averaged geometric mean value of finescale-based estimates of dissipation in the UCDW layer is $4.9 \times 10^{-11} \text{ W kg}^{-1}$, which is similar to that observed. While the uncertainty in strain-based estimates can be as large as a factor of 2, the agreement suggests

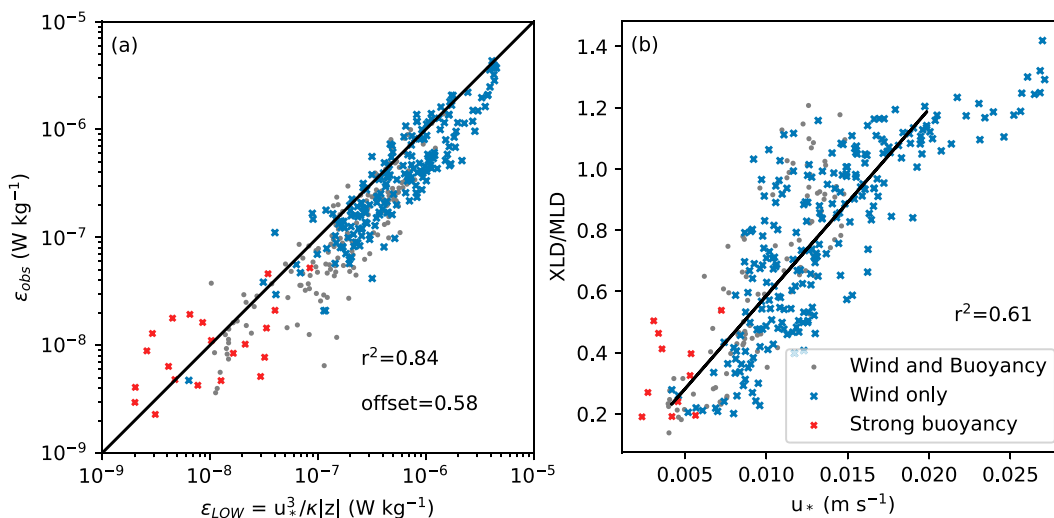


FIG. 5. (a) Relationship between theoretical dissipation rates ε_{LOW} and glider-observed dissipation rates ε_{obs} averaged over 5–15-m depth (on logarithmic scales) during the submesoscale transects of the deployment (25 Dec 2019–22 Jan 2020), corrected for an offset of 0.58. The 1:1 line is plotted for reference in black. (b) Relationship between mixing layer depth [XLD, defined as in Brainerd and Gregg (1995)] normalized by the mixed layer depth MLD and the friction velocity u_* . The symbols are colored according to the dominant forcing, given by the ratio of XLD to L_{MO} . Wind forcing ($\text{XLD}/L_{\text{MO}} < 0.3$) is in blue, strong buoyancy forcing ($\text{XLD}/L_{\text{MO}} > 1$) is in red, and the remainder are in gray dots. A rolling mean over three profiles (~ 4 h) was applied. The black line in (b) is the linear regression (with $r^2 = 0.61$) computed for $\text{XLD}/L_{\text{MO}} < 0.3$ but excluding the points for which the friction velocity is greater than 0.02 m s^{-1} .

that internal waves may account for the background dissipation in the ocean interior. The time-averaged strain-based dissipation estimate in the WW and TL is $4.0 \times 10^{-10} \text{ W kg}^{-1}$. While also comparable to the observations (Table 1), this method does not work well when there is small-scale variation in stratification that is not due to the internal wave field and in regions susceptible to strong DDC (Gregg 1989; Polzin et al. 2014), considered in the following section.

We use similarity scaling to assess the role of wind stress in shear production of turbulence. To a first approximation, the surface of the ocean can be seen as a flat, rigid wall, beneath which a purely shear-driven boundary layer evolves, given by the boundary layer similarity scaling, law of the wall (LOW), which describes the viscous dissipation as decaying with distance from the surface:

$$\varepsilon_{\text{LOW}}(z) = \frac{u_*^3}{\kappa|z|}, \quad (9)$$

where z is the distance from the surface. We reconstruct vertical profiles of turbulent dissipation using the LOW relation. The theoretical dissipation rates predict 84% (Fig. 5a) of the variability in glider-observed dissipation rates (averaged between 5 and 15 m and smoothed over ~ 4 h), indicating that shear-driven turbulence production in this region is largely driven by wind forcing. Outliers at low values of dissipation, marked on Fig. 5a in red, are associated with measurements that were taken when $\text{XLD}/L_{\text{MO}} > 1$ (when buoyancy forcing is strong relative to wind forcing). The markers in blue define where wind forcing is dominant (here defined as $\text{XLD}/L_{\text{MO}} < 0.3$). The threshold of L_{MO} that defines where overturns are driven solely by wind was selected based on the best fit in Fig. 5b, wherein the mixing layer depth deepens

under increasing friction velocity ($r^2 = 0.61$). Mixing layer depth is normalized by the mixed layer depth to identify where the mixing layer deepens below the mixed layer and entrainment can occur. The outliers at high wind stress show that the mixing layer is deepening less than expected (this coincides with the strong wind event centered around 28 December 2019, Fig. 4b). In this case, we see that the mixing depth is deeper than the mixed layer ($\text{XLD}/\text{MLD} > 1$), suggesting entrainment. The vertical extent of mixing is shallower than predicted by LOW alone, because turbulence is suppressed by the stratification at the base of the mixed layer.

2) DOUBLE-DIFFUSIVE CONVECTION

Double-diffusive convection conditions are often found in high latitudes and are characteristic of waters in the Weddell Sea, where the cold, fresh WW overlies warm and salty UCDW (Muench et al. 1990; Shaw and Stanton 2014). A band of DDC conducive conditions was identified where $-\pi/2 < \text{Tu} < -\pi/4$. The average depth range of the DDC band was between 60 and 230 m, in the TL (Fig. 6c). DDC often appears as staircases in the temperature profiles (see example profile in Fig. 6b). Not every profile was characterized by thermohaline staircases, even if the Turner angle indicated that conditions were favorable for DDC to occur and the buoyancy Reynolds number is, on average, lower in the WW and TL (Table 1). Nevertheless, in these cases, it is possible that intermittent energetic turbulent mixing (e.g., from enhanced shear driven by internal waves) prevents the staircase structures from persisting even under DDC conducive conditions (e.g., Guthrie et al. 2017; Shibley and Timmermans 2019). But,

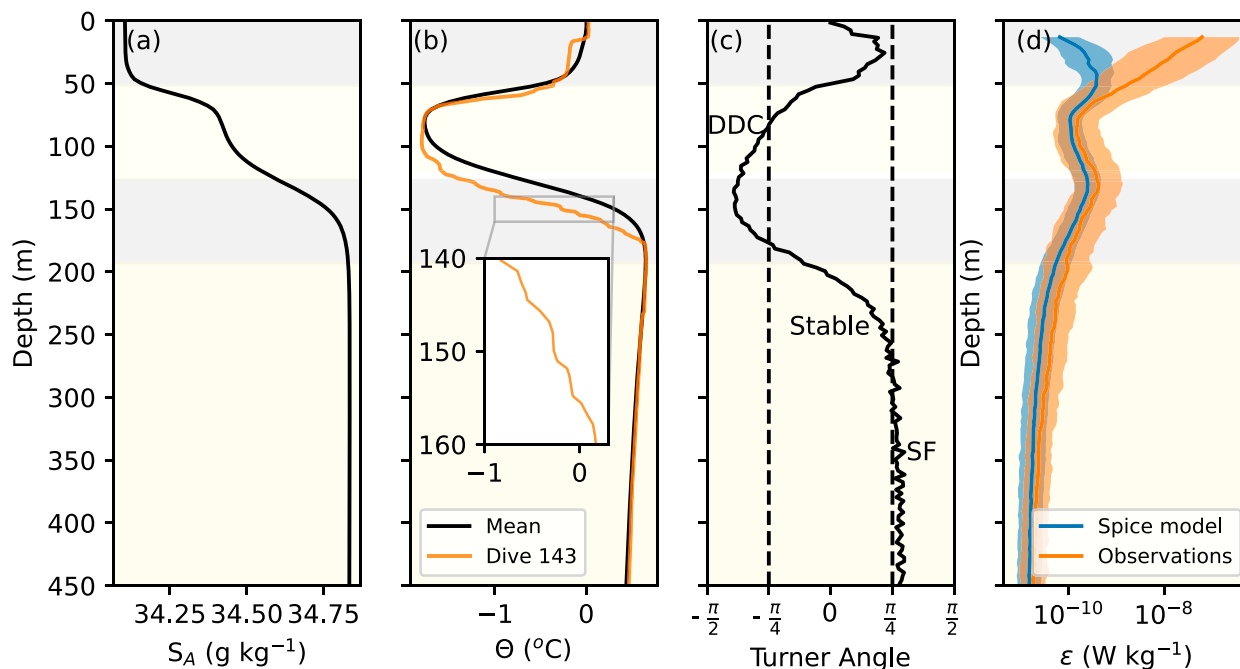


FIG. 6. Mean vertical profiles (of all the subsurface transects) of (a) Absolute Salinity, (b) Conservative Temperature, (c) Turner angle, and (d) geometric mean of predicted dissipation due to double diffusion (blue) and observed (orange) dissipation. Temperature staircases of a characteristic profile of temperature are shown in (b) with a zoom inset between 140 and 160 m. Regions that are susceptible to double-diffusive convection are indicated by vertical dashed lines in (c) and are labeled (DDC: double-diffusive convection; SF: salt-fingering). The shading indicates the mean extent of the ML, WW, TL, and UCDW as in Fig. 2.

considering that the distribution of buoyancy Reynolds number in the WW and TL is skewed to the left (Fig. 3b), shear-driven turbulence in these layers is likely not dominant. Additionally, the glider's average sampling vertical resolution of 0.2 m (1-Hz sampling frequency) means that only temperature staircases with scales larger than 40 cm were resolved, missing finer-scale staircases.

Independent evidence for the likelihood of DDC at the TL is given by the comparative magnitudes and patterns of viscous dissipation parameterized following Middleton et al. (2021) (Fig. 6d). The slight underestimation (a factor of 1.7 on average over 70–180 m) is likely attributable to the additional contribution from intermittent shear-driven dissipation by internal waves.

d. Vertical turbulent heat fluxes into the Winter Water

Turbulent eddies can effectively transport heat across a temperature gradient. The resulting heat flux is approximated based on the rate of turbulent eddy diffusivity and the strength of the vertical gradient (refer to methods section 2f). Because of the characteristic temperature minimum at the core of the subsurface WW layer, the temperature gradient peaks both at the base of the mixed layer and the base of the WW layer (Fig. 2a). At these interfaces, there are also enhanced vertical overturns (high rates of dissipation), which, together with the strong vertical gradient in temperature ($\sim 0.05^\circ\text{C m}^{-1}$), result in the vertical transport of heat. An average heat flux of 15 W m^{-2} from the mixed layer into the WW layer, together with an average of 4 W m^{-2} upward from the underlying UCDW result in a convergence of heat in the subsurface layer (Fig. 7).

In the previous section we find evidence that DDC is driving the observed enhanced layer of dissipation at the base of the WW. The destabilizing buoyancy flux that results from diffusive convection is both a source for TKE and its dissipation, elevating dissipation in an otherwise quiescent environment. Additionally, where DDC is the source of TKE, diffusivity can be estimated using a mixing coefficient of $\Gamma = 1$ because all PE is used to create TKE. Thus, the mixing efficiency of DDC is greater than that resulting from shear production of turbulence by a factor of 5 [see section 2f, Eq. (3)]. The average diffusivity by DDC where $-\pi/2 < \text{Tu} < -\pi/4$ is $(2.5 \pm 0.9) \times 10^{-5} \text{ m}^2 \text{ s}^{-1}$, whereas the average turbulent diffusivity over the same depth range is $(4.5 \pm 1) \times 10^{-6} \text{ m}^2 \text{ s}^{-1}$.

An independent estimate of the double-diffusive contribution to heat flux can be made using the “four-thirds” flux law (Kelley 1990), which was shown to approximate microstructure-based diffusive fluxes well in the Arctic Ocean (Guthrie et al. 2015). We hand selected a number of profiles where thermohaline staircases were well defined and applied the empirical flux law (Kelley 1990),

$$F_{4/3} = 0.0032 \exp\left(\frac{4.8}{R_\rho^{0.72}}\right) \rho_c \left(\frac{\alpha g \kappa_T}{P_r}\right)^{1/3} \Delta T^{4/3}, \quad (10)$$

where R_ρ is the density ratio, $\kappa_T = 1.4 \times 10^{-7} \text{ m}^2 \text{ s}^{-1}$ is the molecular diffusivity of heat for seawater, $P_r = \nu/\kappa$ is the Prandtl number, and ΔT is the temperature difference between adjacent layers. Ungridded 1-s-resolution temperature profiles were used for these calculations. The nondimensional density ratio is a bulk value and was computed from the 3 m gridded data to represent a background average.

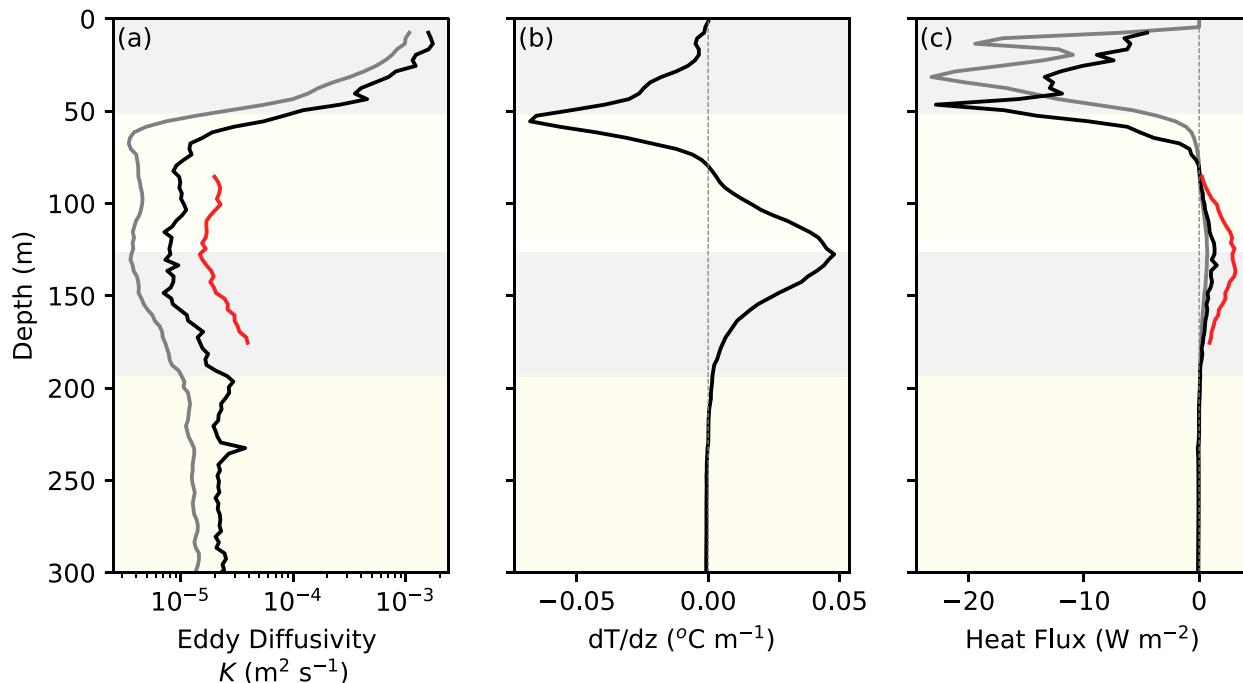


FIG. 7. Mean profiles of (a) eddy diffusivity, (b) vertical temperature gradient, and (c) heat flux. The black lines are the arithmetic means, the gray lines are the geometric means, and the red line is the geometric mean for the double-diffusive case. The gray and yellow shading are defined in Fig. 2.

The mean density ratio [Eq. (6)] for all profiles over the deployment was 2.9 ± 0.3 . For each selected profile, the most defined interface was selected. From this, the mean density ratio and the maximum gradient in temperature were used to compute an upper limit estimate for the flux law, giving an average over 33 selected profiles of $4.7 \pm 1.5 \text{ W m}^{-2}$, which is comparable to the average heat flux computed from dissipation measurements ($4.4 \pm 0.3 \text{ W m}^{-2}$). As such, $F_{4/3}$ can approximate the double-diffusive vertical heat fluxes in this region.

e. Drivers of seasonal warming of Antarctic Winter Water

A WW temperature budget is developed to investigate the drivers of the seasonal warming of the WW layer. The mean temperature in this layer increases by 0.2°C over 28 days (Figs. 1d, 2b, and 8a), even though the incoming solar radiation decreases later in the time series (Fig. 4a). Concurrently, the thickness of the layer reduces by 33 m over the same time period (Figs. 2a and 8c). No significant trend in salinity is observed (Fig. 8b), suggesting that the trend in the thickness of the layer is likely driven by the trend in temperature. The drivers of these trends are likely persistent in time, with glider observations from the same location during the

2018/19 summer season also showing a warming of the WW by 1.1°C over 3 months (du Plessis et al. 2022). Similar warming and thinning trends are observed across the Southern Ocean where WW is present (Fig. 1), suggesting that these mechanisms are also widespread.

Heat into the WW layer originates from both lateral and vertical sources. Because we do not have in situ parallel observations of horizontal flow, the temperature budget is simplified to neglect the lateral components contributing to WW layer variability. Within the sea ice impacted Southern Ocean surface mixed layer, the lateral transport component (e.g., Ekman transport and mixed layer eddy stirring) has been shown to be considerable (Giddy et al. 2021; du Plessis et al. 2022); however, because of the strong stratification at the base of the mixed layer (Figs. 2c,d), we make the assumption that the processes driving the lateral transport are confined to the mixed layer and can reasonably be neglected in the subsurface layer. Vertical sources considered are entrainment through variation in the depth of the mixed layer and the base of the WW layer, turbulent heat fluxes and incoming solar radiation. The heat budget of the WW layer can then be approximated as

$$\begin{aligned}
 \underbrace{\left(\frac{\partial T}{\partial t}\right)_{\text{WW}}}_{\text{Temperature tendency}} &= + \underbrace{\frac{1}{h_{\text{WW}} c_p \rho_o} [Q_{\text{SW(ML)}} - Q_{\text{SW(WW)}}]}_{\text{I: Shortwave radiation}} - \underbrace{\frac{1}{h_{\text{WW}}} \left[\left(-K \frac{\partial T}{\partial z}\right)_{-h_{\text{ML}}} - \left(-K_{\text{DDC}} \frac{\partial T}{\partial z}\right)_{-h_{\text{WW}}}\right]}_{\text{II: Vertical mixing}} \\
 &\quad - \underbrace{\frac{1}{h_{\text{WW}}} \{H(W_{e\text{ML}})(T_{\text{ML}} - T_{\text{WW}}) + H(W_{e\text{WW}})(T_{\text{WW}} - T_{\text{WW}+5})\}}_{\text{III: Vertical entrainment}}. \tag{11}
 \end{aligned}$$

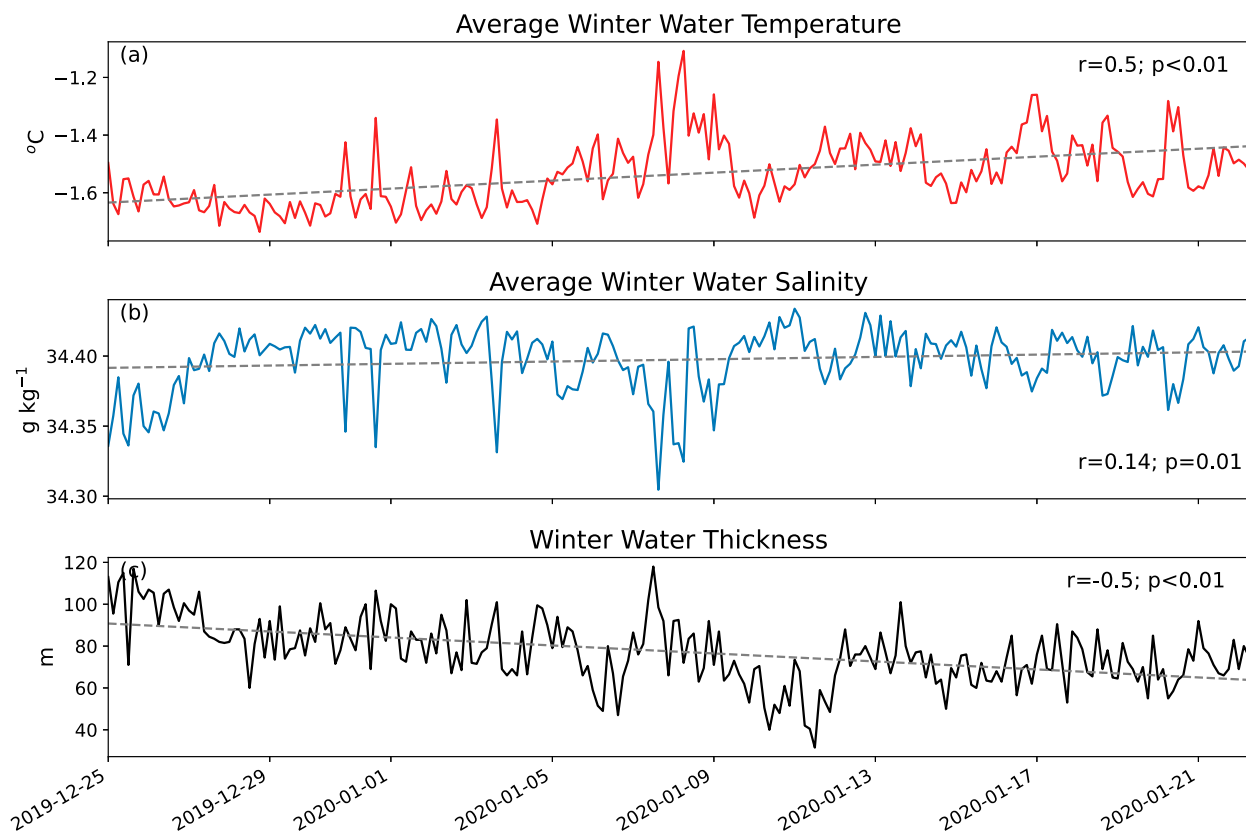


FIG. 8. Temporal evolution of averaged properties within the WW layer are provided for (a) Θ and (b) S_A , along with (c) the WW layer thickness. Marked on (a)–(c) are the trends estimated over the observational period (gray dashed lines); r is the correlation coefficient of the linear regression with time, and $p < 0.01$ shows a significant trend.

Depth is positive upward. T_{ML} is the mean temperature in the mixed layer, T_{WW} is the mean temperature in the WW layer, and h_{WW} is the thickness of the WW layer.

The first term on the right hand side (I) is the accumulation of shortwave radiation Q_{SW} in the WW layer (Fig. 4d). This term is approximated by exponentially decaying the incoming shortwave radiation with depth following Wijesekera (2005), using a double exponential formulation for the decay of penetrative solar radiation for Jerlov Type II waters, applicable for the open ocean where chlorophyll $a > 0.01 \text{ mg m}^{-3}$ (Paulson and Simpson 1977),

$$R_s(z) = R_s(0)[0.77 \exp(-|z|/1.4) + 0.23 \exp(-|z|/14)], \quad (12)$$

where $R_s(0)$ is the net shortwave radiation at the surface and z is depth. The difference in Q_{SW} at the base of the mixed layer and the base of the WW is taken as the accumulated Q_{SW} .

The second term (II) is the vertical mixing term, decomposed into shear-driven mixing at the base of the mixed layer and double-diffusive mixing at the base of the WW layer; K is the eddy diffusivity at the mixed layer base, and K_{DDC} is the eddy diffusivity where DDC is assumed. Also, $(\partial T/\partial z)_{-h_{ML}}$ and $(\partial T/\partial z)_{-h_{WW}}$ are the vertical temperature gradients across the mixed layer and WW interface, respectively. The last term (III) is the entrainment into or detrainment out of the WW layer

from above and below. The vertical velocity across the upper and lower boundaries is computed as $W_e \approx dh/dt$ at each boundary, respectively, assuming negligible Ekman pumping velocities [average $W_{ekman} = (\partial \tau_y/\partial x - \partial \tau_x/\partial y)/(\rho_0 f) \sim 10^{-7} \text{ m s}^{-1}$, two orders of magnitude smaller than the average entrainment velocity at the base of the mixed layer]. H is the Heaviside function, where $W_{eML} < 0$ and $W_{eWW} > 0$ is entrainment and $W_{eML} > 0$ and $W_{eWW} < 0$ is detrainment. $T_{ML} - T_{WW}$ is the difference in mean temperature within the mixed layer and the WW and $T_{WW} - T_{WW+5}$ is the difference in temperature between the average WW temperature and 5 m below the WW base. Vertical entrainment estimates are sensitive to the choice of smoothing for the vertical velocity calculation dh/dt . In this study we selected a 10-h smoothing window (the inertial period at this latitude).

The temperature fluctuations in the WW are resolved by entrainment and detrainment from above and below the mixed layer (e.g., cf. Figs. 9a and 9d); however, the warming trend (Fig. 8a) is explained primarily by the convergence of turbulent heat fluxes (average 19 W m^{-2} into the WW, increasing the temperature by 0.14°C ; Fig. 9c), similar to the warming trend observed in the data (0.2°C ; Fig. 8a). The accumulation of shortwave radiation results in a small additional temperature increase of 0.02°C (2.1 W m^{-2} ; Fig. 9b). The contribution from the shortwave component increases when the mixed layer

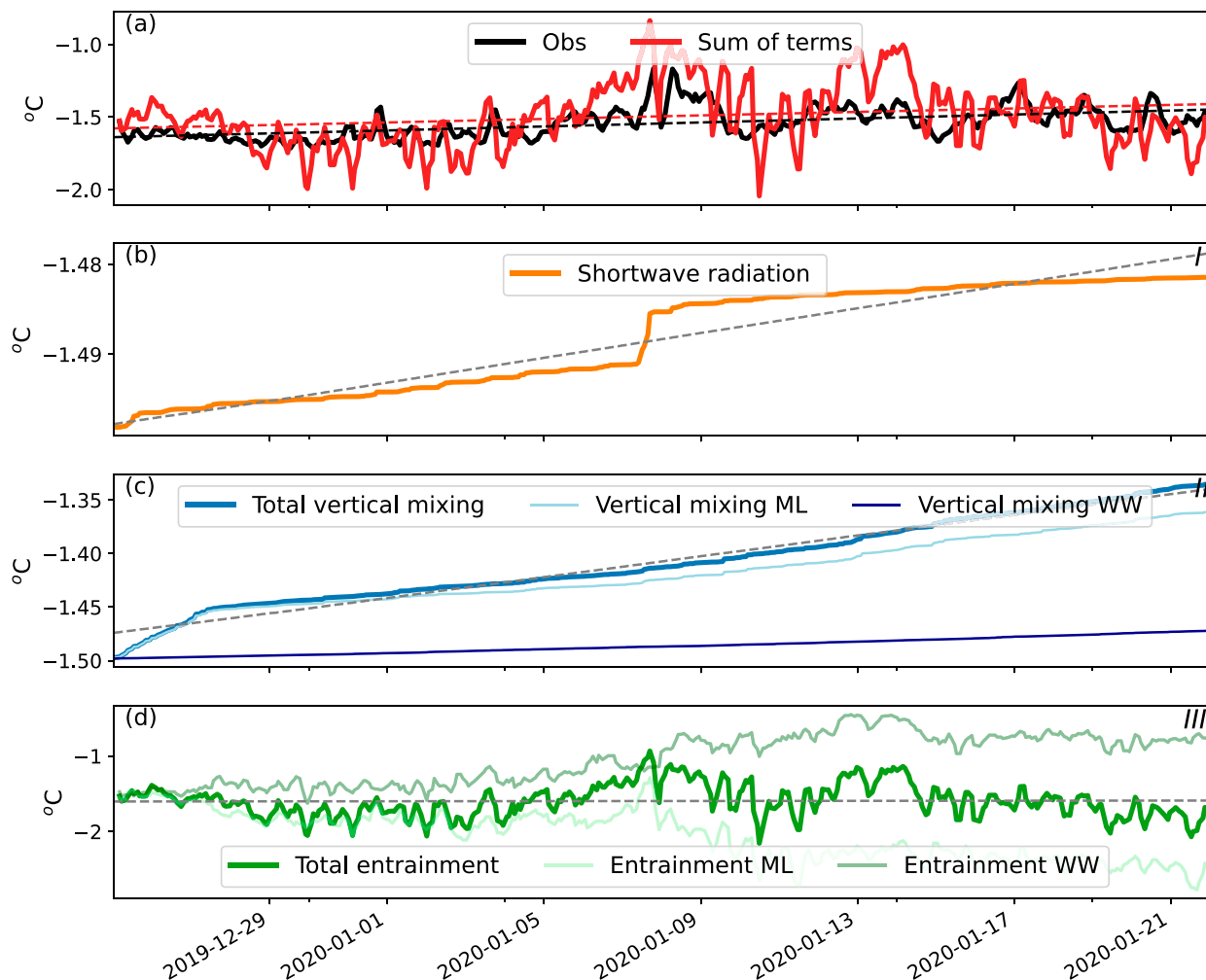


FIG. 9. (a) Observed (black) and modeled (red) WW temperature and the associated components: (b) shortwave radiation; (c) total turbulent vertical mixing (blue), downgradient vertical mixing across the base of the mixed layer (light blue), and upgradient vertical mixing across the base of the WW layer (dark blue); and (d) total vertical entrainment (dark green), detrainment across the base of the mixed layer (green), and entrainment across the base of the WW layer (light green). Trends are indicated by the gray dashed lines on (a)–(d). Note the different scales on the y axes. The roman numerals in the top right of (b)–(d) correspond to the terms in Eq. (11).

shoals (Fig. 4d). It is also likely to increase further during low-concentration phytoplankton blooms or when the bloom terminates (thus changing the exponential decay of shortwave radiation, Giddings et al. 2021). The observed WW temperature trend agrees well with that modeled in the budget (Fig. 9a). Episodic offsets (particularly evident between 13 and 20 January 2020) are likely attributable to some contribution from the lateral components, which is not included in the budget.

4. Discussion and conclusions

This study provides a detailed characterization of the observed turbulent mixing processes in the sea ice impacted Southern Ocean during austral summer. During the period of observation at our study site, recent sea ice melt had stratified the surface layer, capping the cold WW layer between the warm surface

waters and the underlying warm UCDW (Fig. 2). Subsequently, the layer of WW gradually warms and thins over the summer season (Figs. 2 and 8a,c). The subsurface temperature inversion preconditioned a convergence of heat flux into the WW. The setup of a downgradient of heat from the surface mixed layer to the WW and from underlying UCDW to the WW (Figs. 2a,b) was able to explain the warming of the layer over the season (Figs. 7 and 8).

Overall, mechanically driven turbulent mixing accounts for an average of 15 W m^{-2} of heat flux into the WW layer. Assuming DDC drives all the turbulent dissipation at the base of the WW, DDC accounts for a heat flux from the underlying UCDW into the WW layer of $\sim 4 \text{ W m}^{-2}$. While this is an upper estimate, it provides evidence that DDC is likely the primary driver of the upward transfer of heat from the UCDW into the surface layer during austral summer. If DDC is not taken into account (i.e., a mixing coefficient of maximum 0.2 is used) the upward heat flux

would be $<1 \text{ W m}^{-2}$, and result in an underestimation of this term. Moreover, this analysis suggests that most of the observed dissipation that is elevated in the TL is accounted for by DDC (see Fig B1 of appendix B). Therefore not accounting for DDC in this region has the potential to entirely misrepresent this layer of turbulent mixing.

These results suggest that it is the accumulation of heat fluxes into the WW layer via vertical turbulent mixing and DDC that accounts for the seasonal warming trend in the observations (Fig. 9). While the effects of the strong wind event on 28 December 2019 is limited by the magnitude of stratification, the rate of dissipation and therefore eddy diffusivity, is higher and supports enhanced vertical fluxes of heat, temporarily increasing the rate of warming of the WW. This observation indicates that increased frequency of such events will result in a faster transformation rate of the WW. This corroborates with longer term observations in which positive phases of the Southern Annular Mode are linked to warmer WW temperatures (e.g., Sabu et al. 2020).

a. Spatial variability in the seasonal erosion of Winter Water

Although the observations presented here are from a single location, these findings are discussed in the broader spatial context of the WW forming regions of the Southern Ocean (Fig. 1). Observational data products demonstrate that the erosion of WW is not homogeneous across the subpolar Southern Ocean with the Weddell Sea showing some of the most extensive WW erosion (Fig. 1b). Here, regionally weaker stratification predisposes the region to enhanced vertical fluxes (Wilson et al. 2019) that act to erode and limit the vertical extent of WW. Conversely, the Ross Sea and Amundsen–Bellingshausen Sea are regions where a slight broadening of the WW vertical extent and limited warming is observed (Figs. 1b,c). One explanation may be linked to DDC under the presence of weak shear and strong stratification (Bebieva and Speer 2019), where strong stratification between temperature staircases can act as a thermal barrier (Martinson 1990). In this case, well-defined temperature staircases suppress rather than enhance vertical heat fluxes. Further research into the drivers of regional variability in WW evolution is needed to fully understand these patterns, but the observations of regional variability in the summer evolution of the WW layer suggests that there will be a spatially heterogeneous response of the subpolar Southern Ocean to changing wind and sea ice patterns in the future (Young and Ribal 2019; Roach et al. 2020).

b. Southern Ocean significance

WW is a widespread feature of the Southern Ocean (Fig. 1). It forms a barrier between the surface mixed layer and UCDW lying deeper in the water column. As WW warms through the summertime, it tends to thin and erode, bringing the underlying UCDW into closer contact with the surface mixed layer. The processes that drive the erosion of this layer therefore play an important role in mediating the amount of heat and carbon that is exchanged between the deeper, warm and carbon rich UCDW, the surface mixed layer and across the air–sea interface. These observations demonstrate that mixing across the WW layer, and

its subsequent warming, is driven both by surface and subsurface mixing processes. As shown, the convergence of heat into the WW layer is predominantly attributed to two mechanisms: First, wind-driven shear production at the base of the mixed layer (Fig. 5) exchanges warm surface water into the colder WW. Second, DDC (Fig. 6) mixes warm UCDW water upward into the WW. Thus, changes to the rate of upper-ocean mixing have the potential to impact sea ice formation, the exchange of water properties and tracers, and associated water mass transformation. First, strong wind events, through increased turbulent mixing, will act to increase the rate of heat transfer into the WW layer, warm the WW and increase the rate of its erosion. With the observed increase in storm frequency (Young and Ribal 2019), the WW layer may become thinner over the summer season, enhancing heat exchange between the deep and surface ocean. The response of WW to changing large-scale wind patterns has already been observed (Anilkumar et al. 2006; Sabu et al. 2020). These results confirm that the properties of WW can change in response to wind through its impact on turbulent mixing. However, there are many interacting and opposing processes. Stratification is expected to continue to increase (Sallée et al. 2021), suppressing the vertical extent of mixing. Our observations show that heat fluxes may nevertheless be enhanced under strong stratification when wind-driven mixing is enhanced (Fig. 9b). Second, as UCDW warms (Auger et al. 2021), the thermal gradient between UCDW and the overlying WW is expected to increase, enhancing heat flux via DDC in certain subpolar regions. Reduced ice cover would simultaneously decrease the seasonal stratification that results from sea ice melt, allowing heat to be more readily transported to the surface layer, where it inhibits further ice growth (Martinson 1990). An additional mechanism driving turbulence production, not directly addressed here, is given by observations of submesoscale flows in the seasonally ice covered Southern Ocean (Swart et al. 2020; Biddle and Swart 2020; Giddy et al. 2021) that provide evidence for the potential of submesoscale-associated processes to modulate the rates of turbulent dissipation that we observed. In particular, the observed coupling between winds and lateral gradients (Swart et al. 2020) following sea ice melt is suggestive that winds aligned downfront of these submesoscale eddies or frontal meanders may be enhancing dissipation rates (e.g., D’Asaro et al. 2011). Submesoscales can also have an indirect influence on the depth and intensity of boundary layer turbulence by restratifying the mixed layer, although this is likely a small contribution during the meltwater stratified conditions in the summer (Giddy et al. 2021). Future work will seek to better constrain rates of dissipation due to submesoscales in this region.

Previous work has emphasized the importance of variations in surface salinity (linked to sea ice) in regulating the rate of water mass transformation in the subpolar Southern Ocean (Abernathey et al. 2016; Pellichero et al. 2018). Here, we consider that changes in the mechanisms that drive heat flux can contribute to increasing the buoyancy of UCDW and the transformation to Antarctic Intermediate Water before it reaches the mixed layer. Observations show that the Southern Ocean is warming; however, interannual variability in the WW layer south of Australia has been observed to be greater than the long-term trend (Auger et al. 2021, their Fig. 4b). The shoaling and warming trend of the UCDW has been linked to increased

stratification at the base of the WW layer, reducing mixing and the loss of heat from UCDW to overlying waters and the atmosphere (Auger et al. 2021). The increase in stratification is likely linked to freshwater forcing (Marshall et al. 2014; Armour et al. 2016; Lecomte et al. 2017). This work quantifies the contribution of turbulent mixing and its sensitivity to the driving mechanisms in regulating heat fluxes between these two water masses. While DDC may not contribute significantly to the global energy balance (van der Boog et al. 2021), it is identified here as an important mechanism mediating fluxes of heat between UCDW and WW and is therefore an important process for water mass transformation in the subpolar Southern Ocean.

Acknowledgments. Author I. Giddy received support from NRF-SANAP (SNA170506229906), an iAtlantic Horizon 2020 grant (818123), the STINT-NRF Mobility Grant (STNT180910357293) and the Oppenheimer Memorial Trust. Author S. Swart was supported by a Wallenberg Academy Fellowship (WAF 2015.0186) and the Swedish Research Council (VR 2019-04400). Authors S.-A. Nicholson and S. Swart received support from NRF-SANAP (SNA170522231782 and SANAP200324510487). Swart and Nicholson also received funding from the European Union's Horizon 2020 research and innovation program under Grant Agreement 821001 (SO-CHIC). Author I. Fer received support from the Research Council of Norway, through the AROMA project (Grant 294396). The authors thank the captain and crew of the SA *Agulhas II* and the assistance of Sea Technology Services for the deployment, retrieval, and piloting of the Slocum. We thank Dr. Gerd Krahnmann for making the glider data-processing software available and for assistance in the glider processing and Dr. Leo Middleton for sharing the spice parameterization of dissipation routines and discussions thereof. We are also grateful to Prof. Lynne Talley and two anonymous reviewers for their insightful comments on the paper.

Data availability statement. The in situ data are available via Zenodo (<https://10.5281/zenodo.7957942>). ECMWF ERA5 data are generated using Copernicus Climate Change Service Information, available online (<https://www.ecmwf.int/en/forecasts/datasets/archive-datasets/reanalysis-datasets/era5>).

APPENDIX A

Quality Control Measures for Dissipation Rate Estimates

Here we describe the quality control (QC) procedures applied to each dissipation estimate from both shear probes, respectively, to identify dissipation estimates that are deemed untrustworthy. Data that do not pass the QC are masked before the analysis. First, the MR internal clock has a tendency to drift over time. The Slocum clock was used to correct for a 17-s drift in the MR clock over the period of the deployment. The additional procedures are described as follows:

QC1—The servo-controlled battery positioning of the Slocum creates vibrations that may affect the quality of turbulence measurements. The servo was deactivated during the climbs

but not during the dives because of a piloting error. To correct for the servo-caused vibrations, segments during which the servo was on (identified as segments during the dive where the pitch changed) were filtered out from the dataset.

QC2—Turbulence estimates within 20 m of the glider's inflection points are excluded. When the glider inflects, the angle of attack and estimate of glider speed are uncertain. Mechanical vibrations necessary to change the glider pitch at inflection also contaminate the measurements.

QC3—Histograms of the glider angle of attack (AOA), pitch, roll, and speed were used to diagnose the glider flight metrics. AOA and glider speed through the water are estimated from the hydrodynamic model of (Merckelbach et al. 2010), implemented in G. Krahnmann's GEOMAR software. Outliers were hand selected and masked. If the glider AOA is too steep, the data are also not reliable. Data for which the glider's AOA was greater than $|\pm 5^\circ|$ were masked. Pitch angles less than $|\pm 15^\circ|$ and greater than $|\pm 30^\circ|$ were also masked as too-shallow or too-steep pitch angles, respectively. We noted that the pitch and AOA was more consistent on the climbs because the servo control was not deactivated. When the flow past the sensor was less than 0.25 m s^{-1} , the data were masked. Rapid changes in pitch and roll are also unreliable, so data for which ΔRoll and ΔPitch were greater than 1° were masked.

QC4—The shear spectra were averaged over increasing levels of dissipation and compared with the empirical Nasmyth spectra. The figure of merit (FOM), which is a metric for the mean absolute deviation (MAD) from Nasmyth (Wolk et al. 2002), is used to exclude spectra that do not follow the model spectrum. Here, the definition of FOM at the time of processing was $\text{MAD}(\text{DOF})^{1/2}$, where DOF is the degrees of freedom of the spectrum, different than the improved definition now recommended by the ATOMIX working group. Turbulence estimates with $\text{FOM} > 1.5$ are masked. For increasingly weaker dissipation, the threshold is relaxed, such that for dissipation data between 10^{-10} and $10^{-11} \text{ W kg}^{-1}$ a mask is applied where $\text{FOM} > 2$ and for values greater than $10^{-11} \text{ W kg}^{-1}$ a mask is applied where $\text{FOM} > 2.5$.

QC5—All dissipation values greater than $1 \times 10^{-4} \text{ W kg}^{-1}$ are masked because these values are too high to be detectable by the shear probes and can be assumed to be bad data.

QC6—Remaining suspect dissipation estimates were hand-selected and masked.

QC7—To derive one estimate of dissipation from the two shear probes, we compared the dissipation estimates of the shear probes with each other. If their ratio was larger than 5, we selected the minimum value of the two, otherwise the average of the two was taken. Note that this threshold is arbitrary and that ATOMIX has an improved recommendation now that was not available at the time of data processing.

APPENDIX B

Double-Diffusive Dissipation Parameterization

We estimate dissipation by double-diffusive convection based on the theory and method developed by Middleton and

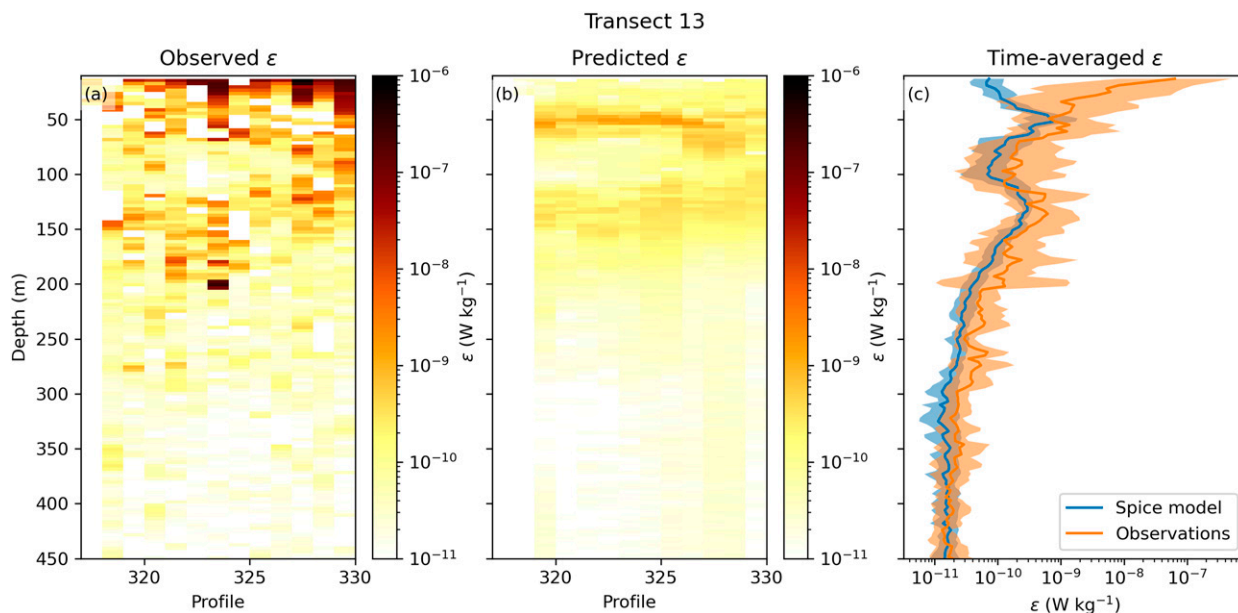


FIG. B1. Example from a single glider transect (transect 13) of (a) observed dissipation and (b) predicted dissipation due to double-diffusive convection. Also shown is (c) the spatially averaged geometric mean and standard deviation of dissipation of observed dissipation (orange) and predicted dissipation (blue).

Taylor (2020) and Middleton et al. (2021). In this method, ε is estimated as

$$\langle \varepsilon \rangle = \frac{\kappa_T + \kappa_S}{2b_z^*} \langle |\Delta b|^2 \rangle + g \frac{\kappa_T - \kappa_S}{2b_z^*} \langle |\Delta b|^2 \rangle \sqrt{\frac{2}{3} + \frac{N^2}{3f^2}} \sqrt{\frac{A}{2}} k_{Oz}, \quad (\text{B1})$$

in which κ_T and κ_S are the molecular diffusivities of heat and salt, respectively; $b = -g[(\rho - \rho_0)/\rho_0]$ is the buoyancy; b_z^* is the gradient of the sorted buoyancy profile; g is acceleration due to gravity; N is the buoyancy frequency; f is the Coriolis frequency; A is the magnitude of the spice gradients; and k_{Oz} is the wavenumber associated with the Ozmidov length scale. The equation is solved iteratively. For a full description and derivation see Middleton et al. (2021).

We applied the method to the glider-observed CTD data for each north-south transect individually. Figure 6d shows the time averaged geometric mean of dissipation across all transects. In this example, below the surface mixed layer, the method effectively reproduces much of the structure in observed ε (Fig. B1). Intermittent high-dissipation events that are not resolved by the parameterization are likely attributable to internal wave-driven turbulence.

REFERENCES

- Abernathy, R. P., I. Cerovecki, P. R. Holland, E. Newsom, M. Mazloff, and L. D. Talley, 2016: Water-mass transformation by sea ice in the upper branch of the Southern Ocean overturning. *Nat. Geosci.*, **9**, 596–601, <https://doi.org/10.1038/ngeo2749>.
- Anilkumar, N., and Coauthors, 2006: Fronts, water masses and heat content variability in the western Indian sector of the Southern Ocean during austral summer 2004. *J. Mar. Syst.*, **63**, 20–34, <https://doi.org/10.1016/j.jmarsys.2006.04.009>.
- Armour, K. C., J. Marshall, J. R. Scott, A. Donohoe, and E. R. Newsom, 2016: Southern Ocean warming delayed by circumpolar upwelling and equatorward transport. *Nat. Geosci.*, **9**, 549–554, <https://doi.org/10.1038/ngeo2731>.
- Auger, M., R. Morrow, E. Kestenare, J.-B. Sallée, and R. Cowley, 2021: Southern Ocean in-situ temperature trends over 25 years emerge from interannual variability. *Nat. Commun.*, **12**, 514, <https://doi.org/10.1038/s41467-020-20781-1>.
- Bebieva, Y., and M.-L. Timmermans, 2016: An examination of double-diffusive processes in a mesoscale eddy in the Arctic Ocean. *J. Geophys. Res. Oceans*, **121**, 457–475, <https://doi.org/10.1002/2015JC011105>.
- , and K. Speer, 2019: The regulation of sea ice thickness by double-diffusive processes in the Ross Gyre. *J. Geophys. Res. Oceans*, **124**, 7068–7081, <https://doi.org/10.1029/2019JC015247>.
- Belcher, S. E., and Coauthors, 2012: A global perspective on Langmuir turbulence in the ocean surface boundary layer. *Geophys. Res. Lett.*, **39**, L18605, <https://doi.org/10.1029/2012GL052932>.
- Biddle, L. C., and S. Swart, 2020: The observed seasonal cycle of submesoscale processes in the Antarctic marginal ice zone. *J. Geophys. Res. Oceans*, **125**, e2019JC015587, <https://doi.org/10.1029/2019JC015587>.
- Bouffard, D., and L. Boegman, 2013: A diapycnal diffusivity model for stratified environmental flows. *Dyn. Atmos. Oceans*, **61–62**, 14–34, <https://doi.org/10.1016/j.dynatmoce.2013.02.002>.
- Brainerd, K. E., and M. C. Gregg, 1995: Surface mixed and mixing layer depths. *Deep-Sea Res. I*, **42**, 1521–1543, [https://doi.org/10.1016/0967-0637\(95\)00068-H](https://doi.org/10.1016/0967-0637(95)00068-H).
- Cheng, L., J. Zhu, R. Cowley, T. Boyer, and S. Wijffels, 2014: Time, probe type, and temperature variable bias corrections to historical expendable bathythermograph observations. *J.*

- Atmos. Oceanic Technol.*, **31**, 1793–1825, <https://doi.org/10.1175/JTECH-D-13-00197.1>.
- D’Asaro, E., C. Lee, L. Rainville, R. Harcourt, and L. Thomas, 2011: Enhanced turbulence and energy dissipation at ocean fronts. *Science*, **332**, 318–322, <https://doi.org/10.1126/science.1201515>.
- de Boyer Montégut, C., G. Madec, A. S. Fischer, A. Lazar, and D. Iudicone, 2004: Mixed layer depth over the global ocean: An examination of profile data and a profile-based climatology. *J. Geophys. Res.*, **109**, C12003, <https://doi.org/10.1029/2004JC002378>.
- Dohan, K., and R. E. Davis, 2011: Mixing in the transition layer during two storm events. *J. Phys. Oceanogr.*, **41**, 42–66, <https://doi.org/10.1175/2010JPO4253.1>.
- du Plessis, M. D., S. Swart, L. C. Biddle, I. S. Giddy, P. M. S. Monteiro, C. J. C. Reason, A. F. Thompson, and S.-A. Nicholson, 2022: The daily-resolved Southern Ocean mixed layer: Regional contrasts assessed using glider observations. *J. Geophys. Res. Oceans*, **127**, e2021JC017760, <https://doi.org/10.1029/2021JC017760>.
- Evans, D. G., J. D. Zika, A. C. Naveira Garabato, and A. J. G. Nurser, 2018: The cold transit of Southern Ocean upwelling. *Geophys. Res. Lett.*, **45**, 13 386–13 395, <https://doi.org/10.1029/2018GL079986>.
- Fer, I., R. Skogseth, and F. Geyer, 2010: Internal waves and mixing in the marginal ice zone near the Yermak Plateau. *J. Phys. Oceanogr.*, **40**, 1613–1630, <https://doi.org/10.1175/2010JPO4371.1>.
- , A. K. Peterson, and J. E. Ullgren, 2014: Microstructure measurements from an underwater glider in the turbulent Faroe Bank channel overflow. *J. Atmos. Oceanic Technol.*, **31**, 1128–1150, <https://doi.org/10.1175/JTECH-D-13-00221.1>.
- Foster, T. D., and E. C. Carmack, 1976: Temperature and salinity structure in the Weddell Sea. *J. Phys. Oceanogr.*, **6**, 36–44, [https://doi.org/10.1175/1520-0485\(1976\)006<0036:TASSIT>2.0.CO;2](https://doi.org/10.1175/1520-0485(1976)006<0036:TASSIT>2.0.CO;2).
- Giddings, J., K. J. Heywood, A. J. Matthews, M. M. Joshi, B. G. M. Webber, A. Sanchez-Franks, B. A. King, and P. N. Vinayachandran, 2021: Spatial and temporal variability of solar penetration depths in the Bay of Bengal and its impact on sea surface temperature (SST) during the summer monsoon. *Ocean Sci.*, **17**, 871–890, <https://doi.org/10.5194/os-17-871-2021>.
- Giddy, I., S. Swart, M. du Plessis, A. F. Thompson, and S.-A. Nicholson, 2021: Stirring of sea-ice meltwater enhances submesoscale fronts in the Southern Ocean. *J. Geophys. Res. Oceans*, **126**, e2020JC016814, <https://doi.org/10.1029/2020JC016814>.
- Good, S. A., M. J. Martin, and N. A. Rayner, 2013: EN4: Quality controlled ocean temperature and salinity profiles and monthly objective analyses with uncertainty estimates. *J. Geophys. Res. Oceans*, **118**, 6704–6716, <https://doi.org/10.1002/2013JC009067>.
- Goodman, L., E. R. Levine, and R. G. Lueck, 2006: On measuring the terms of the turbulent kinetic energy budget from an AUV. *J. Atmos. Oceanic Technol.*, **23**, 977–990, <https://doi.org/10.1175/JTECH1889.1>.
- Gordon, A. L., and B. A. Huber, 1984: Thermohaline stratification below the Southern Ocean sea ice. *J. Geophys. Res.*, **89**, 641–648, <https://doi.org/10.1029/JC089iC01p00641>.
- , and —, 1990: Southern Ocean winter mixed layer. *J. Geophys. Res.*, **95**, 11 655–11 672, <https://doi.org/10.1029/JC095iC07p11655>.
- Gouretski, V., and L. Cheng, 2020: Correction for systematic errors in the global dataset of temperature profiles from mechanical bathythermographs. *J. Atmos. Oceanic Technol.*, **37**, 841–855, <https://doi.org/10.1175/JTECH-D-19-0205.1>.
- Gregg, M. C., 1989: Scaling turbulent dissipation in the thermocline. *J. Geophys. Res.*, **94**, 9686–9698, <https://doi.org/10.1029/JC094iC07p09686>.
- , E. A. D’Asaro, J. J. Riley, and E. Kunze, 2018: Mixing efficiency in the ocean. *Annu. Rev. Mar. Sci.*, **10**, 443–473, <https://doi.org/10.1146/annurev-marine-121916-063643>.
- Guthrie, J. D., I. Fer, and J. Morison, 2015: Observational validation of the diffusive convection flux laws in the Amundsen Basin, Arctic Ocean. *J. Geophys. Res. Oceans*, **120**, 7880–7896, <https://doi.org/10.1002/2015JC010884>.
- , —, and J. H. Morison, 2017: Thermohaline staircases in the Amundsen Basin: Possible disruption by shear and mixing. *J. Geophys. Res. Oceans*, **122**, 7767–7782, <https://doi.org/10.1002/2017JC012993>.
- Hersbach, H., and Coauthors, 2018: ERA5 hourly data on single levels from 1979 to present. Copernicus Climate Change Service (C3S), Climate Data Store (CDS), accessed 2 December 2021, <https://cds.climate.copernicus.eu/cdsapp#!/dataset/reanalysis-era5-single-levels?tab=overview>.
- Hoppema, M., 2004: Weddell Sea is a globally significant contributor to deep-sea sequestration of natural carbon dioxide. *Deep-Sea Res. I*, **51**, 1169–1177, <https://doi.org/10.1016/j.dsr.2004.02.011>.
- Inoue, R., H. Yamazaki, F. Wolk, T. Kono, and J. Yoshida, 2007: An estimation of buoyancy flux for a mixture of turbulence and double diffusion. *J. Phys. Oceanogr.*, **37**, 611–624, <https://doi.org/10.1175/JPO2996.1>.
- Kelley, D. E., 1990: Fluxes through diffusive staircases: A new formulation. *J. Geophys. Res.*, **95**, 3365–3371, <https://doi.org/10.1029/JC095iC03p03365>.
- Krahmann, G., 2023: GEOMAR FB1-PO Matlab Slocum glider processing toolbox. GEOMAR, https://doi.org/10.3289/SW_4_2023.
- Lecomte, O., H. Goosse, T. Fichefet, C. de Lavergne, A. Barthélemy, and V. Zunz, 2017: Vertical ocean heat redistribution sustaining sea-ice concentration trends in the Ross Sea. *Nat. Commun.*, **8**, 258, <https://doi.org/10.1038/s41467-017-00347-4>.
- Marshall, J., K. C. Armour, J. R. Scott, Y. Kostov, U. Hausmann, D. Ferreira, T. G. Shepherd, and C. M. Bitz, 2014: The ocean’s role in polar climate change: Asymmetric Arctic and Antarctic responses to greenhouse gas and ozone forcing. *Philos. Trans. Roy. Soc.*, **A372**, 20130040, <https://doi.org/10.1098/rsta.2013.0040>.
- Martinson, D. G., 1990: Evolution of the Southern Ocean winter mixed layer and sea ice: Open Ocean deepwater formation and ventilation. *J. Geophys. Res.*, **95**, 11 641–11 654, <https://doi.org/10.1029/JC095iC07p11641>.
- McDougall, T. J., and P. M. Barker, 2011: Getting started with TEOS-10 and the Gibbs Seawater (GSW) Oceanographic Toolbox. SCOR/IAPSO WG127, 28 pp., https://www.teos-10.org/pubs/Getting_Started.pdf.
- Merckelbach, L., D. Smeed, and G. Griffiths, 2010: Vertical water velocities from underwater gliders. *J. Atmos. Oceanic Technol.*, **27**, 547–563, <https://doi.org/10.1175/2009JTECHO710.1>.
- Middleton, L., and J. R. Taylor, 2020: A general criterion for the release of background potential energy through double diffusion. *J. Fluid Mech.*, **893**, R3, <https://doi.org/10.1017/jfm.2020.259>.
- , E. C. Fine, J. A. MacKinnon, M. H. Alford, and J. R. Taylor, 2021: Estimating dissipation rates associated with double diffusion. *Geophys. Res. Lett.*, **48**, e2021GL092779, <https://doi.org/10.1029/2021GL092779>.

- Muench, R. D., J. T. Gunn, and D. M. Husby, 1990: The Weddell-Scotia confluence in midwinter. *J. Geophys. Res.*, **95**, 18 177–18 190, <https://doi.org/10.1029/JC095iC10p18177>.
- Nasmyth, P. W., 1970: Oceanic turbulence. Ph.D. thesis, University of British Columbia, 106 pp., <https://doi.org/10.14288/1.0302459>.
- Nicholson, S.-A., D. B. Whitt, I. Fer, M. D. du Plessis, A. D. Lebéhot, S. Swart, A. J. Sutton, and P. M. S. Monteiro, 2022: Storms drive outgassing of CO₂ in the subpolar Southern Ocean. *Nat. Commun.*, **13**, 158, <https://doi.org/10.1038/s41467-021-27780-w>.
- Osborn, T. R., 1980: Estimates of the local rate of vertical diffusion from dissipation measurements. *J. Phys. Oceanogr.*, **10**, 83–89, [https://doi.org/10.1175/1520-0485\(1980\)010<0083:EOTLRO>2.0.CO;2](https://doi.org/10.1175/1520-0485(1980)010<0083:EOTLRO>2.0.CO;2).
- Park, Y.-H., and I. Durand, 2019: Altimetry-driven Antarctic circumpolar current fronts. SEANOE, accessed 7 February 2022, <https://doi.org/10.17882/59800>.
- Paulson, C. A., and J. J. Simpson, 1977: Irradiance measurements in the upper ocean. *J. Phys. Oceanogr.*, **7**, 952–956, [https://doi.org/10.1175/1520-0485\(1977\)007<0952:IMITUO>2.0.CO;2](https://doi.org/10.1175/1520-0485(1977)007<0952:IMITUO>2.0.CO;2).
- Pellichero, V., J.-B. Sallée, S. Schmidtko, F. Roquet, and J.-B. Charrassin, 2017: The ocean mixed layer under Southern Ocean sea-ice: Seasonal cycle and forcing. *J. Geophys. Res. Oceans*, **122**, 1608–1633, <https://doi.org/10.1002/2016JC01970>.
- , —, C. C. Chapman, and S. M. Downes, 2018: The Southern Ocean meridional overturning in the sea-ice sector is driven by freshwater fluxes. *Nat. Commun.*, **9**, 1789, <https://doi.org/10.1038/s41467-018-04101-2>.
- Polzin, K. L., J. M. Toole, and R. W. Schmitt, 1995: Finescale parameterizations of turbulent dissipation. *J. Phys. Oceanogr.*, **25**, 306–328, [https://doi.org/10.1175/1520-0485\(1995\)025<0306:FPOTD>2.0.CO;2](https://doi.org/10.1175/1520-0485(1995)025<0306:FPOTD>2.0.CO;2).
- , A. C. Naveira Garabato, T. N. Huussen, B. M. Sloyan, and S. Waterman, 2014: Finescale parameterizations of turbulent dissipation. *J. Geophys. Res. Oceans*, **119**, 1383–1419, <https://doi.org/10.1002/2013JC008979>.
- Roach, L. A., and Coauthors, 2020: Antarctic Sea ice area in CMIP6. *Geophys. Res. Lett.*, **47**, e2019GL086729, <https://doi.org/10.1029/2019GL086729>.
- Sabu, P., S. A. Libera, R. Chacko, N. Anilkumar, M. P. Subeesh, and A. P. Thomas, 2020: Winter water variability in the Indian Ocean sector of Southern Ocean during austral summer. *Deep-Sea Res. II*, **178**, 104852, <https://doi.org/10.1016/j.dsr2.2020.104852>.
- Sallée, J.-B., and Coauthors, 2021: Summertime increases in upper-ocean stratification and mixed-layer depth. *Nature*, **591**, 592–598, <https://doi.org/10.1038/s41586-021-03303-x>.
- Scheifele, B., S. Waterman, and J. R. Carpenter, 2021: Turbulence and mixing in the Arctic Ocean's Amundsen Gulf. *J. Phys. Oceanogr.*, **51**, 169–186, <https://doi.org/10.1175/JPO-D-20-0057.1>.
- Shaw, W. J., and T. P. Stanton, 2014: Dynamic and double-diffusive instabilities in a weak pycnocline. Part I: Observations of heat flux and diffusivity in the vicinity of Maud Rise, Weddell Sea. *J. Phys. Oceanogr.*, **44**, 1973–1991, <https://doi.org/10.1175/JPO-D-13-042.1>.
- Shibley, N. C., and M.-L. Timmermans, 2019: The formation of double-diffusive layers in a weakly turbulent environment. *J. Geophys. Res. Oceans*, **124**, 1445–1458, <https://doi.org/10.1029/2018JC014625>.
- , —, J. R. Carpenter, and J. M. Toole, 2017: Spatial variability of the Arctic Ocean's double-diffusive staircase. *J. Geophys. Res. Oceans*, **122**, 980–994, <https://doi.org/10.1002/2016JC012419>.
- Shih, L. H., J. R. Koseff, G. N. Ivey, and J. H. Ferziger, 2005: Parameterization of turbulent fluxes and scales using homogeneous sheared stably stratified turbulence simulations. *J. Fluid Mech.*, **525**, 193–214, <https://doi.org/10.1017/S0022112004002587>.
- Song, H., J. Marshall, J.-M. Campin, and D. J. McGillicuddy Jr., 2019: Impact of near-inertial waves on vertical mixing and air-sea CO₂ fluxes in the Southern Ocean. *J. Geophys. Res. Oceans*, **124**, 4605–4617, <https://doi.org/10.1029/2018JC014928>.
- St. Laurent, L., and R. W. Schmitt, 1999: The contribution of salt fingers to vertical mixing in the North Atlantic tracer release experiment. *J. Phys. Oceanogr.*, **29**, 1404–1424, [https://doi.org/10.1175/1520-0485\(1999\)029<1404:TCOSFT>2.0.CO;2](https://doi.org/10.1175/1520-0485(1999)029<1404:TCOSFT>2.0.CO;2).
- Swart, S., M. D. du Plessis, A. F. Thompson, L. C. Biddle, I. Giddy, T. Linders, M. Mohrmann, and S.-A. Nicholson, 2020: Submesoscale fronts in the Antarctic marginal ice zone and their response to wind forcing. *Geophys. Res. Lett.*, **47**, e2019GL086649, <https://doi.org/10.1029/2019GL086649>.
- Toole, J. M., 1981: Sea ice, winter convection, and the temperature minimum layer in the Southern Ocean. *J. Geophys. Res.*, **86**, 8037–8047, <https://doi.org/10.1029/JC086iC09p08037>.
- Turner, J. S., 1973: *Buoyancy Effects in Fluids*. Cambridge University Press, 367 pp.
- van der Boog, C. G., H. A. Dijkstra, J. D. Pietrzak, and C. A. Katsman, 2021: Double-diffusive mixing makes a small contribution to the global ocean circulation. *Commun. Earth Environ.*, **2**, 46, <https://doi.org/10.1038/s43247-021-00113-x>.
- Whalen, C. B., J. A. MacKinnon, L. D. Talley, and A. F. Waterhouse, 2015: Estimating the mean diapycnal mixing using a finescale strain parameterization. *J. Phys. Oceanogr.*, **45**, 1174–1188, <https://doi.org/10.1175/JPO-D-14-0167.1>.
- Wijesekera, H. W., D. L. Rudnick, C. A. Paulson, S. D. Pierce, W. S. Pegau, J. Mickett, and M. C. Gregg, 2005: Upper Ocean heat and freshwater budgets in the eastern Pacific warm pool. *J. Geophys. Res.*, **110**, C08004, <https://doi.org/10.1029/2004JC002511>.
- Wilson, E. A., S. C. Riser, E. C. Campbell, and A. P. S. Wong, 2019: Winter upper-ocean stability and ice-ocean feedbacks in the sea ice-covered Southern Ocean. *J. Phys. Oceanogr.*, **49**, 1099–1117, <https://doi.org/10.1175/JPO-D-18-0184.1>.
- Wolk, F., H. Yamazaki, L. Seuront, and R. G. Lueck, 2002: A new free-fall profiler for measuring biophysical microstructure. *J. Atmos. Oceanic Technol.*, **19**, 780–793, [https://doi.org/10.1175/1520-0426\(2002\)019<0780:ANFFPF>2.0.CO;2](https://doi.org/10.1175/1520-0426(2002)019<0780:ANFFPF>2.0.CO;2).
- Young, I. R., and A. Ribal, 2019: Multiplatform evaluation of global trends in wind speed and wave height. *Science*, **364**, 548–552, <https://doi.org/10.1126/science.aav9527>.